# Southern Ocean abyssal mixing on climatic timescales

K. L. Sheen[1*], A. C. Naveira Garabato[1], J. A. Brearley[1], M. P. Meredith[2], K. L. Polzin[3], D. A. Smeed[3], A. Forryan[1], B. A. King[4], J. B. Sallée[5], L. St. Laurent[3], J. R. Ledwell[3], A. M. Thurnherr[6], J. M. Toole[3], S. N. Waterman[7] & A. J. Watson[8].

[1]*University of Southampton, National Oceanography Centre, Southampton, U.K.;*
[*]*k.sheen@soton.ac.uk*

[2]*British Antarctic Survey, Cambridge, U.K.*

[3]*Woods Hole Oceanographic Institution, Woods Hole, Massachusetts, U.S.A.*

[4]*National Oceanography Centre, Southampton, U.K.*

[5]*Laboratoire d'Océanographie et du Climat, Paris, France.*

[6]*Lamont-Doherty Earth Observatory, Palisades, New York, U.S.A.*

[7]*Climate Change Research Centre and ARC Centre of Excellence for Climate System Science, University of New South Wales, Sydney, Australia.*

[8]*University of Exeter, U.K.*

**The Southern Ocean plays a pivotal role in global ocean circulation and climate [1–3]. It is there that the deep water masses of the world ocean upwell to the surface and subsequently sink to intermediate and abyssal depths, forming two overturning cells that exchange large amounts of heat and carbon with the atmosphere[4–6]. While the climatic drivers of changes in the upper cell are relatively well established[7], little is known about how the lower cell responds to changes in climatic forcing. Here, we show the first observational evidence that**

**small-scale mixing in the abyssal Southern Ocean, a major driver of the lower overturning cell[8–10], exhibits variability on time scales of months to decades, consistent with a significant modulation by oceanic eddies impinging on seafloor topography. As the intensity of the regional eddy field is regulated by the Southern Hemisphere westerlies[11,12], our findings suggest that Southern Ocean abyssal mixing and overturning are sensitive to climatic perturbations in wind forcing.**

The Southern Ocean limb of the global overturning circulation consists of two cells[4,5,13]. The upper cell involves the upwelling and southward flow of mid-depth waters of North Atlantic origin, their transformation into lighter waters within the upper layers of the Antarctic Circumpolar Current (ACC), and their subsequent return northward as mode and intermediate waters. This vertical circulation is underpinned by a combination of wind-driven Ekman motions, eddy-induced flows, and air-sea interaction, which sustains the diabatic near-surface water mass transformation[4,7,14]. In the lower cell, the southward shoaling of mid-depth waters is balanced by the production of dense abyssal waters by intense oceanic heat loss along the Antarctic margin. These abyssal waters are exported northward into and across the ACC and, in the process, are transformed into mid-depth waters by small-scale, turbulent diabatic mixing. Ultimately, it is the intensity of this mixing that sets the rate at which the abyssal ocean overturns[8,9,15].

Observations of the spatial distribution of turbulent mixing[16–20] and idealised modelling studies[15,21] link the occurrence of Southern Ocean abyssal mixing to the breaking of internal lee waves, generated as the ACC's vigorous mesoscale eddy flows impinge on seafloor topography.

The radiation and breaking of lee waves is estimated to account for the bulk of the dissipation of the Southern Ocean eddy field [21,22], and to support a major fraction of the diabatic water mass transformation closing the lower overturning cell in the abyssal ocean [23]. This prompts the hypothesis that Southern Ocean abyssal mixing and overturning are sensitive to the intensity of the regional eddy field and, since the eddy field is primarily energised by instabilities of the wind-forced circulation[8,24,25], to climatic perturbations in atmospheric forcing.

We address this hypothesis by analysing the temporal variability of Southern Ocean abyssal mixing and internal wave properties using a unique collection of repeat measurements of shear microstructure and density finestructure along the SR1b transect, which crosses the ACC in Drake Passage (Figure 1). These measurements consist of: three repeat shear microstructure sections (conducted in April 2011, February/March 2012 and March 2013) under the auspices of the Diapycnal and Isopycnal Mixing Experiment in the Southern Ocean, DIMES (see http://dimes.ucsd.edu), from which the spatial distribution of the rate of dissipation of turbulent kinetic energy ($\epsilon$, a metric of the intensity of small-scale turbulence) is computed; and of twenty repeat density finestructure sections (conducted quasi-annually between November 1993 and March 2013), from which $\epsilon$ is estimated using a finescale parameterization[20,28,29]. The results of these calculations are interpreted in the context of satellite altimetric observations of surface kinetic energy anomaly ($\mathrm{KE}_{anom}$), and by reference to a 2-year (December 2009 - March 2012) mooring record of $\mathrm{KE}_{anom}$ and abyssal internal wave shear (from which $\epsilon$ is estimated with a finescale parameterization analogous to that above) with daily resolution in northern Drake Passage (Figure 1). The mooring data were also obtained as part of DIMES [30]. Details of all data sets and calculations are provided in the Methods section.

The temporal variability in small-scale turbulence across Drake Passage is illustrated by Figure 2, showing profiles of $\epsilon$ and current speed for the three repeat microstructure sections. Turbulent dissipation in the northern half of the SR1b section is generally elevated relative to the southern half, as expected from the rougher topography in the northern region[16,20]. $\epsilon$ values to the south of the Polar Front (PF) approach background levels ($\epsilon = O(10^{-10})$ W kg$^{-1}$) below the upper-ocean mixed layer, and patches of enhanced dissipation rates ($\epsilon = O(10^{-9})$ W kg$^{-1}$) are found consistently over the northern continental slope. Elsewhere, substantial section-to-section variations are apparent: in April 2011, dissipation levels to the north of the PF are elevated by up to one order of magnitude ($\epsilon \sim 10^{-9}$ W kg$^{-1}$) relative to the other two sections ($\epsilon \sim 10^{-10}$ W kg$^{-1}$), and exhibit a more pronounced near-bottom enhancement. This difference occurs in association with a general intensification of near-bottom flows in April 2011, and stems from microstructure profiles collected within areas of relatively high near-bottom speed associated with the eddying frontal jets of the ACC (see Suppl. Mat.). These observations suggest that changes in near-bottom eddy flow underpin the observed temporal variability of turbulent dissipation in the Drake Passage abyss, through the generation and breaking of internal waves.

This interpretation is endorsed by two complementary lines of evidence. First, a significant correlation exists between the measured near-bottom speed and microstructure-derived abyssal dissipation (Figure 2, Suppl. Mat.), pointing to a link between the two variables. Application of wave radiation theory[17,20] to the observations of near-bottom flow during the three repeat microstructure sections confirms that the intensification of the flow in April 2011 is sufficient to account for the order-of-magnitude enhancement in dissipation documented at that time (see Suppl. Mat.). Secondly, the 2-year mooring record of finestructure-derived abyssal dissipation in northern Drake Passage exhibits variability spanning two orders of magnitude ($\epsilon = 2\,\mathrm{x}\,10^{-10}\,\mathrm{W\,kg^{-1}}$ to $\epsilon = 250\,\mathrm{x}\,10^{-10}\,\mathrm{W\,kg^{-1}}$, Figure 3a), that is significantly correlated and energetically consistent with the near-bottom eddy flow speed[30]. The mooring dissipation rate time-series also reveals that the April 2011 microstructure section was obtained during a 6-month period in which abyssal dissipation was enhanced by a factor of ~2.5 relative to early 2012, just prior to the subsequent microstructure transect occupation.

The changes in near-bottom eddy flow underpinning variations in abyssal turbulence are not exclusively a deep-ocean phenomenon, but are part of a mode of eddy variability that is evident throughout the water column. This is illustrated by the analysis of the vertical structure in the spectral coherence between abyssal dissipation and $\mathrm{KE}_{anom}$ (see Methods) at the DIMES mooring site. Fluctuations in abyssal dissipation with periods of 1-3 months, characteristic of the eddy field, are significantly coherent with $\mathrm{KE}_{anom}$ changes in the deepest $\sim 1000$ m and uppermost $\sim 400$ m of the water column, but incoherent with fluctuations in mid-depth $\mathrm{KE}_{anom}$ (see Supp. Mat.). This pattern of coherence reflects the first-baroclinic modal structure typically exhibited by eddy motions with a prominent near-bottom and surface manifestation, which corresponds to the second empirical orthogonal function (EOF2) of $u$ and $v$ (see Suppl. Mat.). It results in abyssal dissipation being significantly correlated not only with near-bottom $\mathrm{KE}_{anom}$ and altimetry-derived surface $\mathrm{KE}_{anom}$ (Figures 3, S8 & S10), but also with $\mathrm{KE}_{anom}$ derived from EOF2 of the velocity field [30] (Suppl. Mat.). The energization of first-baroclinic mode eddy flows is a predicted effect of baroclinic instability[33], and may be expected to enhance abyssal dissipation through the promotion of internal wave generation by intensified near-bottom eddy flow[15,17,19,20,22] and of internal wave breaking through critical layer interactions[31].

The existence of a surface footprint of near-bottom eddy activity in Drake Passage allows us to assess the mechanisms underpinning abyssal turbulent dissipation variability over longer, climatically relevant time scales (years to decades). A 20-year time series of finestructure-derived abyssal dissipation (Figure 4a) reveals a similar spatial pattern to that in the microstructure data (Figure 2): consistently elevated dissipation ($\epsilon \sim \ 30\,\mathrm{x}\,10^{-10}\,\mathrm{W\,kg^{-1}}$) near the northern edge of Drake Passage, over the South American continental slope; lower dissipation ($\epsilon \sim \ 3\,\mathrm{x}\,10^{-10}\,\mathrm{W\,kg^{-1}}$) south of 58.5°S, where topography is relatively smooth and eddy variability is weak; and highly variable dissipation in between. There is a sharp transition between intense and weak dissipation that migrates meridionally between section occupations and spans the 57°S - 58.5°S latitude range. Significantly, this transition tracks closely the position of the meandering PF jet, as might be expected if abyssal dissipation were modulated by eddy flow with both surface and bottom expressions. The same relationship is evident in a comparison between time series of finestructure-derived abyssal dissipation within the latitude band of the PF and altimetric surface $\mathrm{KE}_{anom}$ (Figures 4b & S13). While surface $\mathrm{KE}_{anom}$ is highly variable, a record of $\mathrm{KE}_{anom}$ values extracted at the times of occupation of the SR1b section exhibits a significant correlation with $\epsilon$ (r = 0.6, $p < 0.01$) that is robust to modest variations in the latitude band over which data is averaged. Note that the reduction in finestructure-derived dissipation and surface $\mathrm{KE}_{anom}$ between April 2011 and March 2012/2013 is consistent with the microstructure observations (Figure 2).

Global maps of altimetric surface eddy kinetic energy (EKE, the average of $\mathrm{KE}_{anom}$ over many eddy time scales) indicate that the SR1b transect is embedded within a region of elevated EKE (Figure 1). It has been shown that EKE in this and other ACC areas around major topographic obstacles is modulated by changes in wind forcing on interannual-to-interdecadal time scales, largely by major climatic modes such as the Southern Annular Mode (SAM) and El Niño - Southern Oscillation [11,12,32], (Supp. Mat., Figure S14). While this climatic modulation is evident in EKE averaged over the wider Drake Passage region, the nature of the eddy field's response to a forcing perturbation is both nonlocal and highly patchy on length scales comparable to those of the eddies (O(100 km)). As a result, a relationship between large-scale forcing and EKE along the SR1b section (or any other similarly sized line across the ACC) is not expected, and the evolution of local $\mathrm{KE}_{anom}$ over the last two decades is instead dominated by stochastic variability with time scales of weeks to months (Figure 4b). However, since the fundamental physics linking eddy flows to deep-ocean turbulent dissipation is common to all ACC regions of rough topography [15,17–20], the sensitivity of Southern Ocean EKE to changes in forcing is indicative of a climatic modulation of abyssal mixing in the region.

This study represents the first evidence that variability of Southern Ocean abyssal mixing on time scales of months to decades is modulated by mesoscale eddies, via the breaking of internal waves generated as deep-reaching eddy flows impinge on seafloor topography. The Southern Ocean eddy field is primarily energised by instabilities of the wind-forced ACC [8,24,25] and, as such, its kinetic energy is sensitive to climatic perturbations in the Southern Hemisphere westerlies[11,12,32]. It thus follows that the intensity of Southern Ocean abyssal mixing must be similarly reactive to climatic modulation. Motivated by the recent and projected interdecadal intensification of the westerlies[35,36], many authors have investigated the eddy-mediated response of the upper cell of global overturning to changes in Southern Ocean wind forcing[37,38]. As Southern Ocean abyssal mixing is a major driver of the lower overturning cell[8,9,15,39], our findings suggest that this circulation is likely to be regulated by the westerlies, and that the dynamical coupling between winds, eddies and abyssal mixing unveiled here must be factored into investigations of the climatic evolution of deep-ocean overturning.

# Methods

**SR1b repeat hydrographic section.** In situ conductivity-temperature-depth (CTD) and, for some occupations, lowered acoustic Doppler current profiler (LADCP) data, are available along the World Ocean Circulation Experiment (WOCE) SR1b repeat section. This section has been conducted quasi-annually in austral spring / summer since November/December 1993. Microstructure measurements were also collected in the April 2011, March 2012 and March 2013 repeats. Cruise reports and details of processing and uncertainties can be found at `http://noc.ac.uk/drake-passage` and `http://dimes.ucsd.edu/results` [20,42].

**Microstructure estimates of turbulent dissipation along the SR1b section.** The rate of turbulent kinetic energy dissipation, $\epsilon$, was determined directly along three occupations of the SR1b section using free-falling vertical microstructure profilers (VMPs). These instruments record velocity shear, $\partial u/\partial z$, on centimeter scales. Assuming isotropy, the dissipation rate was computed as $\epsilon = 15\mu/2\overline{(\partial u/\partial z)^2}$, where $\mu$ is the molecular viscosity[18–20,40]. Two Rockland Scientific International (http ://www.rocklandscienticfic.com) VMP- 5500 microstructure profilers were used during the DIMES SR1b section occupations, operated by scientists from the National Oceanography Centre, Southampton and the Woods Hole Oceanographic Institution. A careful comparison of instrument noise levels and data processing routines was carried out to ensure no systematic bias between the instruments. Microstructure velocity shear spectra were integrated between frequencies of 10 Hz and that associated with the spectral minimum at frequencies lower than 25 Hz (or 100 Hz for $\epsilon > 10^{-7}\,\mathrm{W\,kg^{-1}}$). Velocity shear variances were calculated every 0.5 m, using bin widths of 1 s (where the sampling rate of the instruments is 512 Hz). Computed dissipation rates were subsequently interpolated onto a 2-m grid. Each instrument carried two shear probes, and unless one was observed to be particularly noisy, the mean of the dissipation estimates from the two probes was used in this analysis. At most stations, data were collected to within 100 m of the sea floor. Microstructure cast locations were recorded as the mid-point between the instrument deployment and recovery positions, with profiler drift being rarely more than a few kilometres.

**Finestructure estimates of turbulent dissipation along the SR1b section.**

$\epsilon$ was also estimated indirectly along each occupation of the SR1b section by applying a finescale parameterization[?,29] to CTD-derived strain. The physical basis of the parameterization is that turbulent dissipation is the end result of a downscale energy cascade driven by nonlinear interactions in the internal wave field, where the cascade is assumed to extend from vertical scales of O(100 m) characteristic of internal waves and measured by the ADCP, to the small (O(1 m)) scales characteristic of the isotropic turbulence ensuing from wave breaking. Details of the calculation procedure are given by [20], so only the most notable parameter choices are reviewed here. Strain spectra were computed in overlapping 512-m segments, and integrated over vertical wavelengths of 60 - 180 m. An average spatial distribution of the shear-to-strain ratio, a metric of the frequency content of the internal wave field, was computed as a mean in latitude - depth space of the values estimated from sixteen SR1b repeats in which both CTD measurements of density and LADCP observations of velocity were obtained (Figure S11). Finescale estimates of $\epsilon$ along each SR1b section occupations were subsequently binned onto a $1^\circ$ (latitude) $\times$ 1 m (depth) grid.

**DIMES mooring array data and analysis.** A 10.5 km $\times$ 10.5 km array of six moorings was deployed close to the northern end of the SR1b line between 12 December 2009 and 5 March 2012 [30] (Figure 1). Velocity measurements from 12 current meters (with 15-minute temporal resolution) installed at depths ranging from 425 m to 3600 m in the central mooring, and from a downward-looking ADCP (with 30-minute temporal resolution) ensonifying the depth range 2800 - 3300 m in the same mooring, are analysed in this work to characterise the vertical structure of $\mathrm{KE_{anom}}$. The mooring was also instrumented with SeaBird MicroCAT CTDs at the same vertical levels as the current meters.

Velocity data from all instruments were quality-controlled as described by [30], and the KE anomaly calculated in 15-minute time steps as $\mathrm{KE}_{anom} = [(u-\overline{u})^2+(v-\overline{v})^2]/2$, where the overbar indicates the time mean over the mooring deployment period. For time-series and correlations shown in Figures 3 and S8, $KE_{anom}$ was low-pass filtered using a 6th-order Butterworth filter and a cut-off frequency of 45 days, thus removing near- and super-inertial variability associated with unbalanced motions (e.g. tides and internal waves). A sensitivity study showed correlations of $KE_{anom}$ with abyssal $\epsilon$ is robust for cut-off frequencies between 30 and 100 days (Figure S10a). The zonal velocity, $u$, and meridional velocity, $v$, time series were decomposed into their EOF components (Figure S10b). $KE_{anom}$ was subsequently computed from time series of $u$ and $v$ for the first three modes, and tested for coherence with abyssal $\epsilon$ (Figures S10c and S3). This method enables the modulation of dissipation rates by the background velocity depth structure to be directly analysed.

Velocity shear data from the moored ADCP and estimates of the buoyancy frequency over the vertical range ensonified by that instrument (where the density gradient entering the buoyancy frequency calculation was computed by first-differencing in depth the closest moored CTD-measured density records at 2100 and 3400 m) were combined in a finescale parameterization to estimate a time series of the rate of abyssal turbulent kinetic energy dissipation[28,29]. Details of the calculation are given in [30], so only the most notable parameter choices are reviewed here. Buoyancy-normalised shear was integrated over vertical wavelengths of 130 - 320 m and, lacking high-vertical-resolution stratification data for the mooring deployment period, the shear-to-strain ratio was set to a constant value (4.5) determined form CTD / LADCP measurements obtained in the mooring region during a 16-station survey in December 2010 [20].

**Computation of surface kinetic energy anomaly and eddy kinetic energy from satellite altimetry data.** Satellite altimeter-derived mean sea level anomaly data were obtained from *ssalto/duacs* (distributed by *AVISO*, available at `ftp.aviso.oceanobs.com`) on a 1/3° Mercator grid at 7-day intervals. The merged, referenced, delayed-time data set was used. The zonal, $u$, and meridional, $v$, components of the surface geostrophic velocity anomaly were calculated from sea level anomaly gradients, and the surface kinetic energy anomaly, $\mathrm{KE_{anom}}$, was computed as $\mathrm{KE_{anom}} = [(\mathrm{u} - \overline{\mathrm{u}})^2 + (\mathrm{v} - \overline{\mathrm{v}})^2]/2$, where the overbar represents the time mean since the start of December 1993, corresponding to the time of the first SR1b hydrographic section occupation. Altimetric surface $\mathrm{KE_{anom}}$ values obtained in 1994 are highlighted differently in Figures 4 and S14, as at this time the ERS satellite was in its geodetic mission, possibly leading to an artificial reduction of surface $\mathrm{KE_{anom}}$ by up to $\sim$30% [41]. Note that in comparing to mooring-derived sub-surface $\mathrm{KE_{anom}}$ records (e.g., Figure 3), satellite velocity anomalies were calculated by reference to the record mean over the 2-year mooring deployment period (12 December 2009 - 5 March 2012), rather than over the 20-year altimetric time series.

# References


1. Toggweiler, J. R. & Russell, J. Ocean circulation in a warming climate. *Nature* **451,** 286–288 (2008).

2. Skinner, L. C., Fallon, S., Waelbroeck, C., Michel, E. & Barker, S. Ventilation of the deep southern ocean and deglacial $CO_2$ Rise. *Science* **328,** 1147–1151 (2010).

3. Rintoul, S. & Naveira Garabato, A. C. Ocean Circulation and Climate: A 21st century perspec-

tive *International Geophysics* **Chapter. 18,** 471–491 (2013).

4. Speer, K., Lumpkin, R. & Sloyan, B. The Diabatic Deacon Cell. *J. Phys. Oceanogr.* **30,** 3212–3222 (2000).

5. Lumpkin, R. & Speer, K. Global Ocean Meridional Overturning *J. Phys. Oceanogr.* **37,** 2550–2562 (2007).

6. Lauderdale, J.M, Naveira Garabato, A. C, Oliver, K. I. C, Follows, M.J. & Williams R. G. Wind-driven changes in Southern Ocean residual circulation, ocean carbon reservoirs and atmospheric $CO_2$ *Clim. Dyn.* **41,** 2145–2164 (2013).

7. Marshall, J & Speer, K. Closure of the meridional overturning circulation through Southern Ocean upwelling. *Nature Geosci.* **5,** 171–180 (2012).

8. Wunsch, C. & Ferrari, R. Vertical mixing, energy, and the general circulation of the oceans. *Ann. Rev. Fluid Mech.* **36,** 281–314 (2004).

9. Ito, M., & Marshall, J. Control of Lower-Limb Overturning Circulation in the Southern Ocean by Diapycnal Mixing and Mesoscale Eddy Transfer. *J. Phys. Oceanogr.* **38,** 2832–2845 (2008).

10. Nikurashin, M. & Vallis, R. A Theory of Deep Stratification and Overturning Circulation in the Ocean. *J. Phys. Oceanogr.* **41,** 485–502 (2011).

11. Meredith, M. P & Hogg, A. M. Circumpolar response of Southern Ocean eddy activity to a change in the Southern Annular Mode *Geophys. Res. Lett.* **33,** L16608 (2006).

12. Morrow, R., Ward, M. L, Hogg, A. M, & Pasquet, S. Eddy response to Southern Ocean climate modes *J. Geophys. Res.*. **115,** C10030 (2010).

13. Naveira Garabato, A. C., Williams, A. P. & Bacon, S. The three-dimensional overturning circulation of the Southern Ocean during the WOCE era *Progress in Oceanogr.* **In press,** (2013).

14. Sloyan, B. & Rintoul, S. R. The Southern Ocean Limb of the Global Deep Overturning Circulation. *J. Phys. Oceanogr.* **31,** 143–173 (2001).

15. Nikurashin, M., Vallis, R. & Adcroft A. Routes to energy dissipation for geostrophic flows in the Southern Ocean. *Nature Geosci.* **6,** 48–51 (2013).

16. Naveira Garabato, A. C., Polzin, K., King. B., Heywood, K. & Visbeck, M. Widespread intense turbulent mixing in the Southern Ocean *Science,* **303,** 210–213 (2004).

17. Nikurashin, M., & R. Ferrari Radiation and dissipation of internal waves generated by geostrophic motions impinging on small-scale topography: Application to the Southern Ocean. *J. Phys. Oceanogr.* **40,** 2025–2042 (2010).

18. St. Laurent, L., Naveira Garabato, A. C., Ledwell, J. R., Thurnherr,A. M., Toole, J. M. & Watson, A. J. Turbulence and Diapycnal Mixing in Drake Passage. *J. Phys. Oceanogr.* **42,** 2143–2152 (2012).

19. Waterman, S., Naveira Garabato, A. C. & Polzin, K. Internal waves and turbulence in the Antatctic Circumpolar Current. *J. Phys. Oceanogr.* **43,** 259–282 (2013).

20. Sheen, K. L., Brearley, J. A., Naveira Garabato, A. C., Smeed, D. A., Waterman, S., Ledwell, J. R., Meredith, M. P., St. Laurent, L., Thurnherr, A. M., Toole, J. M., & Watson, A. J. Rates and mechanisms of turbulent dissipation and mixing in the Southern Ocean: Results from the Diapycnal and Isopycnal Mixing Experiment in the Southern Ocean (DIMES). *J. Geophys. Res. - Oceans* **118,** 1–19 (2013).

21. Nikurashin, M., & R. Ferrari Radiation and dissipation of internal waves generated by geostrophic motions impinging on small-scale topography: Theory. *J. Phys. Oceanogr.* **40,** 1055-1074 (2010).

22. Scott, R. B., Goff, J. A., Naveira Garabato, A. C. & Nurser, A. J. G. Global rate and spectral characteristics of internal gravity wave generation by geostrophic flow over topography. *J. Geophys. Res.,* **116,** C09029 (2011).

23. Nikurashin, M., & R. Ferrari Overturning circulation driven by breaking internal waves in the deep ocean. *Geophys. Res. Lett.* **40,** 3133–3137 (2013).

24. Smith, K. S. Eddy Amplitudes in Baroclinic Turbulence Driven by Nonzonal Mean Flow: Shear Dispersion of Potential Vorticity. *J. Phys. Oceanogr.,* **37,** 1037–1050 (2007).

25. Ferrari, R. & Wunsch, C. Ocean Circulation Kinetic Energy: Reservoirs, Sources, and Sinks. *Annu. Rev. Fluid Mech.,* **41,** 253–282 (2009).

26. Smith, W. H. F. & Sandwell, D. T. Global seafloor topography from satellite altimetry and ship depth soundings. *Science* **277,** 1956 – 1962 (1997).

27. Orsi, A. H., T. Whitworth III, D. Worth, & W. D. Nowlin Jr. On the meridional extent and fronts of the Antarctic Circumpolar Current. *Deep-Sea. Res. I* **42,** 641–673 (1995).

28. Polzin, K. L., Toole, J. M. & Schmitt, R. W. Finescale parameterizations of turbulent dissipation, *J. Phys. Oceanogr.,* **25,** 306–328 (1995).

29. Gregg, M. C., Sanford,T. B. & Winkel, D. P. Reduced mixing from the breaking of internal waves in equatorial waters. *Nature,* **422,** 513–515 (2003).

30. Brearley, J. A., Sheen, K. L., Naveira Garabato, A. C., Smeed, D. A. & Waterman, S. Eddy-induced modulation of turbulent dissipation over rough topography in the Southern Ocean *J. Phys. Oceanogr.* **43,** 2288–2308 (2013).

31. Jones W. L. Propagation of internal gravity waves in fluids with shear flow and rotation. *J. Fluid Mech.,* **30,** 439–448 (1967)

32. Thompson, A. F. & Naviera Garabato, A. C. Equilibration of the Antarctic Circumpolar Current by standing meanders *?*. **?** In review. (2013).

33. Venaille, A. M, Vallis, G. K. & Smith, K. S. Baroclinic Turbulence in the Ocean: Analysis with Primitive Equation and Quasigeostrophic Simulations. *J. Phys. Oceanogr.* **41,** 1605–1606 (2011).

34. Hurrell, J. W. & van Loon, H. A modulation of the atmospheric annual cycle in the Southern Hemisphere. *Tellus A* **46,** 325–338 (1994).

35. Yin, J. A consistent poleward shift of the storm tracks in simulations of 21st century climate. *Geophys. Res. Lett.* **32,** L18701, (2005).

36. Thompson, W. J. & Soloman, S. Interpretation of Recent Southern Hemisphere climate change *Science* **296** 895–899 (2002).

37. Hallberg, R. & Gnanadesikan, A. The role of eddies in determining the structure and response of the wind-driven Southern Hemisphere overturning: results from the modeling eddies in the souther ocean (meso) project. *J. Phys. Oceanogr.* **36,** 2232–2252 (2006).

38. Abernathey, R., Marshall, J. & Ferreira, D. Dependence of southern ocean overturning on wind stress. *J. Phys. Oceanogr.* **41,** 2261–2278 (2011).

39. Stanley, G. J. & Saenko, O. A. Bottom-Enhanced Diapycnal Mixing Driven by Mesoscale Eddies: Sensitivity to Wind Energy Supply. *J. Phys. Oceanogr.* **In press,** 10.1175/JPO-D-13-0116.1 (2013).

40. Oakey, N. S. Determination of the rate of dissipation of turbulent energy from simultaneous temperature and velocity shear microstructure measurements, J. Phys. Oceanogr. **12** 256–271 (1982).

41. Ducet, N., Le Traon, P. Y. and Reverdin, G. Global high-resolution mapping of ocean circulation from TOPEX/Poseidon and ERS-1 and -2 *J. Geophys. Res.* **105,** 19,477–19,498 (2000).

42. Naveira Garabato, A. C., L. Jullion, D. P. Stevens, K. J. Heywood, & B. A. King. Variability of subantarctic mode water and Antarctic intermediate water in the Drake Passage dur-

ing the late Twentieth and early Twenty First Century. *J. Clim.* **22,** 3661–3688, doi:10.1175/2009JCLI2621.1 (2009).

**Acknowledgements** KLS was supported by the ...... School of Ocean and Earth Sciences Contribution Number XXXX.

Reprints and permissions information is available at www.nature.com/reprints

There are no competing financial interests

Correspondence and requests for materials should be addressed to K.Sheen@soton.ac.uk

# Supplementary Material

**Microstructure data noise.** Direct estimates of the turbulent kinetic energy dissipation rate, $\epsilon$, were computed along the SR1b repeat section using microstructure data collected during three research cruises (see Methods). In interpreting differences between these three sets of $\epsilon$ estimates as arising from temporal variability, it is necessary to first assess the contribution of cruise-to-cruise variations in instrumental noise. In short, variations in instrumental noise make a negligible contribution to the measured changes in $\epsilon$ between the three section occupations. Vertical shear spectra for all three microstructure data sets are in good agreement with the universal Nasmyth spectrum of the shear associated with 3-d small-scale turbulence over a range of $\epsilon$ values (Figure S1). While elevated spectral noise levels are present in the April 2011 data for frequencies exceeding $\sim$ 50 Hz (likely due to a modest enhancement in instrument vibration), we note that this effect is only of significance above the upper frequency cut-off of 25 Hz to which microstructure velocity shear spectra are integrated when estimating $\epsilon$ (see Methods). Further to this high-frequency instrumental noise issue, the microstructure data obtained in April 2011 had a slightly higher signal floor ( $\epsilon\sim\ 0.3\,\mathrm{x}\,10^{-10}\,\mathrm{Wkg}^{-1}$) than data collected in March 2012 and March 2013 ($\epsilon\sim\ 0.1\,\mathrm{x}\,10^{-10}\,\mathrm{Wkg}^{-1}$) (Figure S2). A Monte Carlo analysis, in which all $\epsilon$ values less than $\epsilon=\ 0.3\,\mathrm{x}\,10^{-10}\,\mathrm{Wkg}^{-1}$ were set to this threshold value before re-averaging the data into 20-m depth bins, confirmed that the slightly lower signal floor in the April 2011 data set does not affect our estimated $\epsilon$ values significantly (Figure S3). Note also that no finestructure estimates of $\epsilon<\ 0.3\,\mathrm{x}\,10^{-10}\,\mathrm{Wkg}^{-1}$ were obtained in the April 2011 section (Figure S12), suggesting that the higher microstructure signal floor at that time may be of physical origin.

**Temporal variability in near-bottom flow and turbulent dissipation.** The difference between the rates of turbulent dissipation derived from microstructure measurements along the SR1b section in April 2011 and those in later years (Figure 2) is striking. A similar difference is found between finestructure estimates of $\epsilon$ in the three section occupations (Figures 3a & S12). Here we present further evidence that the observed section-to-section changes in abyssal turbulent dissipation have a physical basis.

First, abyssal turbulent dissipation rates are found to co-vary with variations in the intensity of the near-bottom flow, suggesting that the changing rate of generation and breaking of internal lee waves underpins the variability in $\epsilon$. Thus, a significant correlation exists between microstructure-derived abyssal $\epsilon$ and LADCP-measured near-bottom current speed across all three section occupations (Figure S4), and both variables are generally elevated in April 2011 relative to March 2012 and March 2013 (Figure 2). The enhancement of abyssal turbulent dissipation in April 2011 occurs in areas of notable near-bottom flow associated with the eddying frontal jets of the ACC, and not in the relatively quiescent regions between the jets. This point is illustrated by Figure S5, where vertical profiles of $\epsilon$ and current speed are compared for two stations that were occupied both in April 2011 and in March 2012. In one of these stations, similar current speeds were measured in both years, and the observed rates of turbulent dissipation did not change substantially. In the other, abyssal turbulent dissipation was elevated by typically one order of magnitude in April 2011, in conjunction with an enhancement in current speed across much of the water column. Note that the stratification at these illustrative stations did not change appreciably between the two occupations. Further evidence of the focussing of temporal variations of abyssal $\epsilon$ in the ACC jets is given by Figure S6, showing two sets of mean profiles of $\epsilon$ (grouped according to a near-bottom current speed criterion indicative of the presence or absence of a jet) for each of the three SR1b section occupations with microstructure measurements. An enhancement of mean $\epsilon$ in April 2011 is only apparent for the group of profiles sampled within jets.

Second, we apply wave radiation theory to our measurements of small-horizontal-scale (O(1-10 km), the range of horizontal wavelengths implicated in internal lee wave generation [21] topography and near-bottom current speed and stratification to show that the observed variations in the abyssal flow are energetically consistent with the measured changes in abyssal dissipation. Details of the theory, data and calculation procedure are discussed in [20]. Topographic spectral parameters along the SR1b section are computed from high-resolution multibeam bathymetry data, and near-bottom current speed and stratification from LADCP and CTD measurements, respectively, over the deepest 500 m of each station. The station-mean internal wave energy fluxes predicted by this calculation for each section occupation are compared with the station-mean depth-integrated (within 2000 m of the sea bed) $\epsilon$ measured in that transect (Figure S7). A substantially greater (by a factor of $\sim 10$) internal wave energy flux is predicted to have occurred in April 2011 than at the times of the other sections. This is a sufficiently ample enhancement to support the elevated (by a factor of $\sim 4$) abyssal dissipation rates observed in April 2011. Note that the wave radiation calculation predicts energy fluxes that regularly exceed the measured abyssal turbulent dissipation rates. This discrepancy has been previously reported in other regions of the ACC[19,20], and has been suggested to relate to limitations in the representation of topographic blocking effects in wave radiation theory.

**Relationship between surface kinetic energy and abyssal turbulent dissipation at the DIMES mooring site.** The central mooring in the DIMES array included twelve current meters spanning the 425 - 3600 m depth range. Data from these instruments were combined with satellite altimetric measurements of surface geostrophic velocity in an analysis of the kinetic energy anomaly ($KE_{anom}$) throughout the water column and its co-variability with ADCP shear-derived abyssal turbulent dissipation (see Methods). To complement the illustration of the relationship between these variables in Figure 3, scatter plots of surface $KE_{anom}$, abyssal $\mathrm{KE}_{\mathrm{anom}}$ and abyssal $\epsilon$ are shown in Figure S8, annotated with the correlation coefficient and p-value characterising the relationship between each pair of variables. Surface $KE_{anom}$ is found to exhibit a significant relationship (at the 99% level) with both abyssal $\mathrm{KE}_{\mathrm{anom}}$ and $\epsilon$, respectively accounting for 37% and 19% of the variance in each of these two variables.

In contrast, there is no significant association between temporal variability in abyssal turbulent dissipation and $\mathrm{KE}_{\mathrm{anom}}$ in the 400 - 2500 m depth range. This is apparent in Figure S9a, which displays the spectral coherence between abyssal $\epsilon$ and $\mathrm{KE}_{\mathrm{anom}}$ throughout the water column. Abyssal turbulent dissipation is only significantly coherent with $\mathrm{KE}_{\mathrm{anom}}$ in the upper ocean and at depths exceeding 2500 m, on time scales of 40-80 days characteristic of the mesoscale eddy field. Dynamical insight into this pattern of coherence may be obtained by decomposing the velocity time series of $u$ and $v$ into empirical orthogonal functions (EOFs), and re-calculating $\mathrm{KE}_{\mathrm{anom}}$ for each EOF (see Methods). Despite accounting for 71% and 73% of the variance in $u$ and $v$, respectively, EOF1 has an equivalent barotropic-like vertical structure with a weak near-bottom footprint (Figure S9c), and therefore is only weakly coherent with abyssal $\epsilon$ (Figure S9b). In turn, EOF2 accounts for only a relatively minor fraction (15% for $u$ and 18% for $v$) of the variance in the velocity, yet it has a vertical structure resembling the first baroclinic mode, for which the amplitude of the resulting $\mathrm{KE}_{\mathrm{anom}}$ response is largest at the surface and bottom (Figure S9e). As a result, it is EOF2 that primarily underpins the pattern of coherence between $\mathrm{KE}_{\mathrm{anom}}$ and abyssal dissipation (cf. Figures S9a and S9d), as well as the relationships between surface $\mathrm{KE}_{\mathrm{anom}}$, abyssal $\mathrm{KE}_{\mathrm{anom}}$ and abyssal $\epsilon$ synthesised by Figure S8. We also note that it is the meridional velocity component, $v$, which appears to dominate the observed coherence between $\mathrm{KE}_{\mathrm{anom}}$ and $\epsilon$.

As a final note, Figure S10 shows composite maps of altimetric surface $\mathrm{KE}_{\mathrm{anom}}$ in Drake

Passage, constructed by grouping periods of anomalously high or low ADCP shear-derived abyssal turbulent dissipation. Consistent with the preceding findings, the occurrence of elevated abyssal turbulent dissipation at the mooring site is associated with an intensification of surface flow across the northern passage region, whereas weak dissipation is linked to a widespread reduction in the kinetic energy of the circulation across the passage.

**Comparison of microstructure- and finestructure-based estimates of turbulent dissipation.** Finestructure-based estimates of $\epsilon$ are obtained by applying a finescale parameterization to CTD-derived estimates of strain (see Methods). The parameterization's skill is maximised if information on the frequency content of the internal wave field is entered to the parameterization [28]. This information is encapsulated in the shear-to-strain ratio, $R_\omega$, which may be directly estimated only when concurrent CTD and LADCP data are available. Since this is not the case for all twenty SR1b section occupations, we estimate a mean $R_\omega$ field along the SR1b section using CTD and LADCP data from the transects in which both were collected (Figure S11). Comparatively low shear-to-strain ratios are found in the northern half of the section ($R_\omega \sim 5$), with greater ratios ($R_\omega \sim 10$) south of 58 °S. This diagnostic indicates that the internal wave field in the northern half of the section, where the topography is rougher, is dominated by relatively high-frequency, bottom-sourced waves[19,20]. In turn, the lower shear-to-strain ratios in the southern half of the section suggest a prevalence of wind-generated near-inertial waves in that area. While there are inevitable sizeable uncertainties in finestructure-based estimates of $\epsilon$, a comparison with microstructure-derived estimates for the three SR1b section occupations in which both types of data were obtained suggests that finescale estimates capture the important spatio-temporal patterns in turbulent dissipation, despite being biased high by typically half an order of magnitude (Figure S12). As in the case of microstructure-derived estimates, finescale estimates of abyssal $\epsilon$ exhibit a significant relationship with surface $KE_{anom}$ (Figure S13).

**Climatic modulation of surface EKE.** Global maps of altimetric surface EKE reveal that the SR1b section is embedded within a region of elevated mesoscale eddy activity (Figure 1a). Past studies have shown that EKE in this and other ACC sectors of complex topography is modulated by the major modes of Southern Hemisphere climate variability, such as El Niño - Southern Oscillation and the Southern Annular Mode (SAM)[11,12,32]. This modulation is evident, for example, in the widespread increase in EKE in 2000-2003, which followed the SAM-related intensification of the Southern Hemisphere westerlies (denoted by an increase in the SAM index) in 1998-2000 (Figures S14a-b). The spatial footprint of this and other large-scale responses of EKE to the westerlies encompasses the Drake Passage region, thereby indicating that EKE around the SR1b section is reactive to climatic changes in wind forcing. Note, however, that the phase and amplitude of the EKE anomaly associated with any given climatic forcing event is both non-local and highly variable on spatial scales comparable to those of the eddies, being shaped by local topography, details of the mean flow structure and proximity to large standing meanders[12,32]. As a result, the eddy field's large-scale response to a specific forcing perturbation is only apparent in averaging over oceanic regions encompassing many eddy length scales. The patchy nature of the eddy field's response explains, for example, the lack of a clear peak in surface $KE_{anom}$ at the SR1b section between 1999 and 2003 (Figure 4b). In general, however, an intensification of the westerlies leads to a widespread strengthening of the eddy field across Drake Passage (Figure S14c).

**Figure 1** a) Altimetric surface eddy kinetic energy (EKE) across the ACC (see Methods) between 1993 and 2013. The rectangular box indicates the region considered in this study, shown in (b). (b) Surface EKE in Drake Passage (colour shading), with thin grey lines indicating isobaths at 1000 m intervals [26]. The dashed black line marks the SR1b section, and the white star the location of the DIMES mooring array. The solid black lines show the mean positions of the Subantarctic (SAF) and Polar (PF) fronts [27].

**Figure 2** (a) LADCP-measured current speed, $U$, along the SR1b section occupied in April 2011. Black lines indicate neutral density surfaces, contoured every 0.2 kg m$^{-3}$, and the solid black area denotes submarine topography [26]. The black triangles on the upper margin mark the ACC frontal positions. No data is available in gray regions. (b) & (c) As for panel a, but for sections occupied in March 2012 and in March 2013, respectively. (d) Vertical profiles of microstructure-derived $\epsilon$ for the SR1b section occupation in April 2011. The blue circles on the upper margin mark the five co-located stations (see Figures S2, S4 & S6). (e) & (f) As for panel d, but for SR1b section occupations in March 2012 and in March 2013, respectively.

**Figure 3** (a) Time series of abyssal ($\sim$ 3300 m) $\epsilon$ (thin grey line) at the DIMES mooring site (located close to 56$^\circ$ S on the SR1b section, Figure 1c). $\epsilon$ is estimated by applying a finescale parameterization to daily averaged moored ADCP shear measurements (see Methods). The data gap in December 2010 is associated with the mooring turn-around half-way through the deployment. The thick black line shows the $\epsilon$ time series after it has been low-pass filtered using a 6th-order Butterworth filter with a cut-off frequency of 45 days. The red and blue arrows respectively mark the times of the section occupations in April 2011 (Figures 2a & 2d) and the SR1b repeat section conducted in November/December 2011 (Figure 4). The vertical blue bars have a width of 20 days, and indicate enhanced dissipation events. (b) Time series of low-pass filtered (using the same filter as in (a)) altimetric surface kinetic energy anomaly, $\mathrm{KE}_{\mathrm{anom,surf}}$ (thick black line), and of the surface expression of the $\mathrm{KE}_{\mathrm{anom}}$ computed from second velocity EOFs (thick blue line, see Methods). (c) Time series of low-pass filtered (using the same filter as in (a) and (b)) abyssal kinetic energy anomaly derived from the deepest moored current meter, at $\sim$ 3600 m ($\mathrm{KE}_{\mathrm{anom,3600m}}$, thick black line), and of the near-bottom expression of the second EOF of $\mathrm{KE}_{\mathrm{anom}}$ (thick blue line, see Methods). The correlation coefficient, $R$, and significance level, $p$, value for correlations between the variables in each panel are indicated (see also Suppl. Mat.).

**Figure 4** (a) Abyssal $\epsilon$ (mean $\epsilon$ value within 2 km of the sea bed, estimated by applying a finescale parameterization to CTD-derived strain data; see Methods and Suppl. Mat.) along the SR1b section, displayed as a function of latitude and time. The double-headed black arrow bounds the region between the SAF and PF (defined as the region in which the difference in the geopotential anomaly between 100 db and 1000 db falls between 4.5 $\mathrm{m}^3\,\mathrm{kg}^{-}1$ and 8.5 $\mathrm{m}^3\,\mathrm{kg}^{-}1$). The dashed lines show the latitude limits of the region used in constructing the time series of average $\epsilon$ in (b). (b) Time series of altimetric surface KE$_{\mathrm{anom}}$ averaged over a $3^{\circ} \times 3^{\circ}$ box centred on 58.5° S, 57.5° W and low-pass filtered with a 90-day cut-off filter (thin blue line, see Methods). The thick blue line and circles highlight the altimetric surface $KE_{\mathrm{anom}}$ at the times of SR1b section occupations. The open circle and dashed lines denote the time when the ERS satellite was in its geodetic mission (leading to an artificial reduction in $KE_{\mathrm{anom}}$ by up to $\sim$30% during 1994 [41]). The thick yellow line and circles indicate the abyssal $\epsilon$ averaged between 57° S and 60° S along the SR1b line, as shown in (a). Open circles and dashed lines indicate times when some CTD stations in the averaging region were not occupied. Correlation $R$ and $p$ values between abyssal $\epsilon$ and surface $KE_{\mathrm{anom}}$ are indicated (see also Suppl. Mat.).

**Figure 5** **S1** (a) Microstructure-deduced vertical shear spectra (black lines), collected using the VMP along SR1b section during April 2011 (DIMES UK2.5 cruise). The spectra are averaged into five dissipation rate bins, equally spaced in log space between $\epsilon = 10^{-11}$ W kg$^{-1}$ and $\epsilon = 10^{-6}$ W kg$^{-1}$. The number of spectra in each dissipation bin are indicated and the cut-off frequency of 25 Hz, below which the spectral minima is extracted to determine upper spectral integration limit is shown by a vertical dashed line (see Methods). Gray lines show the corresponding theoretical Nasmyth curves. (b) and (c) As for panel (a) but for microstructure data collected during March 2012 data (DIMES UK3 cruise) and March 2013 (DIMES UK4 cruise), respectively.

**Figure 6** **S2**: (a) Distribution of April 2011 microstructure turbulent dissipation rates from five co-located stations along SR1b repeat section (for station locations see blue circles in Figures 2d–2f). (b) and (c) As for panel a but for microstructure data collected in March 2012 and March 2013, respectively.

**Figure 7** **S3**: (a) Turbulent dissipation rates as a function of depth for April 2011, averaged over the five co-located stations (think blue line). For station locations, see blue circles in Figures 2d–2f. $\epsilon$ values were averaged into 20 m depth bins before computing section average. The thin black line shows the dissipation depth profile in which $\epsilon$ values below the noise threshold of $0.3 \, \mathrm{x} \, 10^{-10}$ W kg$^{-1}$ are set to this value, before depth-bin averaging. (b) and (c) As for panel (a), but for five stations collected in March 2012 and March 2013, respectively.

**Figure 8** **S4**: Relationship between mean current speed within 500 m of the seabed, $< U_{500m} >$, and mean dissipation within bottom 2 km, $< \epsilon_{200m} >$, for all SR1b microstructure profiles (Figure 2). Correlation $R$ and $p$ values and line of best fit are indicated.

**Figure 9** **S5** (a) Microstructure-deduced turbulent dissipation rates as a function of depth at 56.8 °S recorded during April 2011 (black line) and March 2012 (gray line). (b) LADCP current speed profile corresponding to dissipation profiles in panel (a). (c) & (d) As for panels (a) & (b), but for a stations located at 55.8°S on the SR1b section.

**Figure 10** **S6** (a) Section mean microstructure deduced turbulent dissipation as a function of height-above-bottom (HAB) for stations with bottom speeds less than 0.1 m s$^{-1}$. The red line corresponds to data collected in April 2011, the blue line to data collected in March 2012 and the green line to March 2013 data. Shaded regions show 95% confidence levels from bootstrapping. Note that $\epsilon$ values less than noise threshold of $0.3 \,\mathrm{x}\, 10^{-10}$ W kg$^{-1}$ are set to that level. (b) As for panel a but for microstructure stations with strong bottom current flow ($>=$ 0.1 m s$^{-1}$).

**Figure 11** **S7** Lee wave radiated power, $P$, computed from linear radiation theory for the three SR1b sections during which microstructure measurements were made (black bars). $P$ values represent the mean value for the stations in which CTD, LADCP and microstructure were collected. The mean power dissipated through turbulent motions in bottom 2000 m for the same set of stations is shown by the gray bars for each year.

**Figure 12** **S8** (a) Regression between altimetry-deduced surface kinetic energy anomaly, KE$_{\mathrm{anom,surf}}$, and ADCP-derived abyssal turbulent dissipation, $\epsilon$, at the DIMES mooring site. The corresponding time-series are shown in Figure 3. Correlation $R$ and $p$ values are indicated, and account for loss degrees-of-freedom due to the 45 day low time pass-filtering of data. (b) Correlation between abyssal turbulent dissipation rates at mooring site and co-located KE anomaly at 3600 m depth, KE$_{\mathrm{anom,3600m}}$, computed from moored-current meter. $R$ and $p$ values indicated. (c) Relationship between surface and abyssal KE anomaly, at the DIMES mooring site.

**Figure 13** **S9** (a) Surface KE$_{\mathrm{anom}}$ field averaged over times when mooring-abyssal turbulent dissipation estimates were enhanced (upper 10% of $\epsilon$ values). The mean position of sub-Antarctic Front (SAF) and Polar Front (PF) are indicated by the black lines [27] and the location of the DIMES mooring array by the black star. (b) As for panel (a) but showing $\mathrm{KE_{anom}}$ for times of low abyssal turbulent dissipation estimates at DIMES mooring site (lower 10% of $\epsilon$ values).

**Figure 14** **S10** (a) Contour plot of spectral coherence between abyssal turbulent dissipation rates computed from moored-ADCP shear spectra, $\epsilon$, and the KE anomaly from 12 mooring current meters, surface altimetry data and depth-mean moored-ADCP velocity estimates. The black contour indicates the 95% significant level and the horizontal black lines marks the pressure levels at which $\mathrm{KE_{anom}}$ was computed. (b) Vertical structure of the first three EOF modes for the zonal current speed , $u$, (dashed lines) and zonal current speed, $v$(solid lines). The barotropic mode (EOF1) is shown in red, the first baroclinic mode (EOF2) in blue and and EOF3 in green. The percentage of the velocity variance which each mode accounts for is indicated on the panel (values are for the mean of $u$ and $v$ contributions). (c) Depth averaged spectral coherence between the time series of moored-ADCP abyssal turbulent dissipation rates, and the KE$\mathrm{KE_{anom}}$ computed from EOF1(red), EOF2(blue) and EOF3(green) components of $u$ and $v$. The black dashed line marks the 95% significant level.

**Figure 15** **S11** Spatially smoothed shear-to-strain ratio, $R_\omega$, field along the SR1b section. Values shown are averaged across all SR1b sections for which both LADCP and CTD data were recorded [20] (see Methods). The seabed is shown by the solid black region.

**Figure 16** **S12** Microstructure estimates of turbulent dissipation, $\epsilon$, versus strain-deduced dissipation rates, $\epsilon_{strain}$, for April 2011 (red), March 2012 (blue) and March 2013 (green) DIMES SR1b section. The one-to-one relationship is shown by the dashed black line. A shear-to-strain ratio of 5 is used for all $\epsilon_{strain}$ estimates (see Methods). The correlation $R$ and $p$ regression values for all three years of data are shown.

**Figure 17** **S13** Relationship between the surface $\mathrm{KE_{anom}}$ and the abyssal turbulent dissipation estimates (in the bottom 2000 m), averaged between 57°S and 60°S for 1993-2012. The corresponding time series is shown in Figure 4b. Open circles highlight the years when the full data set was not available, whilst the gray circles corresponds to data from 1994 when TOPEX/ Poseidon data alone were used in the merged multi-satellite product [41]. The regression line is shown by the solid black line and the correlation $R$ and $p$ values are indicated.

**Figure 18** **S14** (a) Southern Annular Mode (SAM) index, which exhibits a strong peak between late 1997 and mid-2001 (blue bar). Data was obtained from http://www.nerc-bas.ac.uk/public/icd/gjma/. (b) Annual mean of EKE anomaly in the Pacific sector (dashed) and SR1b region (solid). The boxes in panel (c) show the sector locations. The blue band highlights enhanced levels between late 1999 and late 2002, believed to be a lagged response to 1998-2002 SAM index peak [11,12]. (c) Altimetry-deduced surface EKE anomaly between mid-1999 and 2002, chosen to correspond with EKE peak shown in panel (b). The dashed and solid boxes mark the Pacific and SR1b averaging regions, shown in panel (b), respectively. Although the signal is spatially patchy, regions of strong positive anomalies correspond to regions of high EKE (Figure 1a).

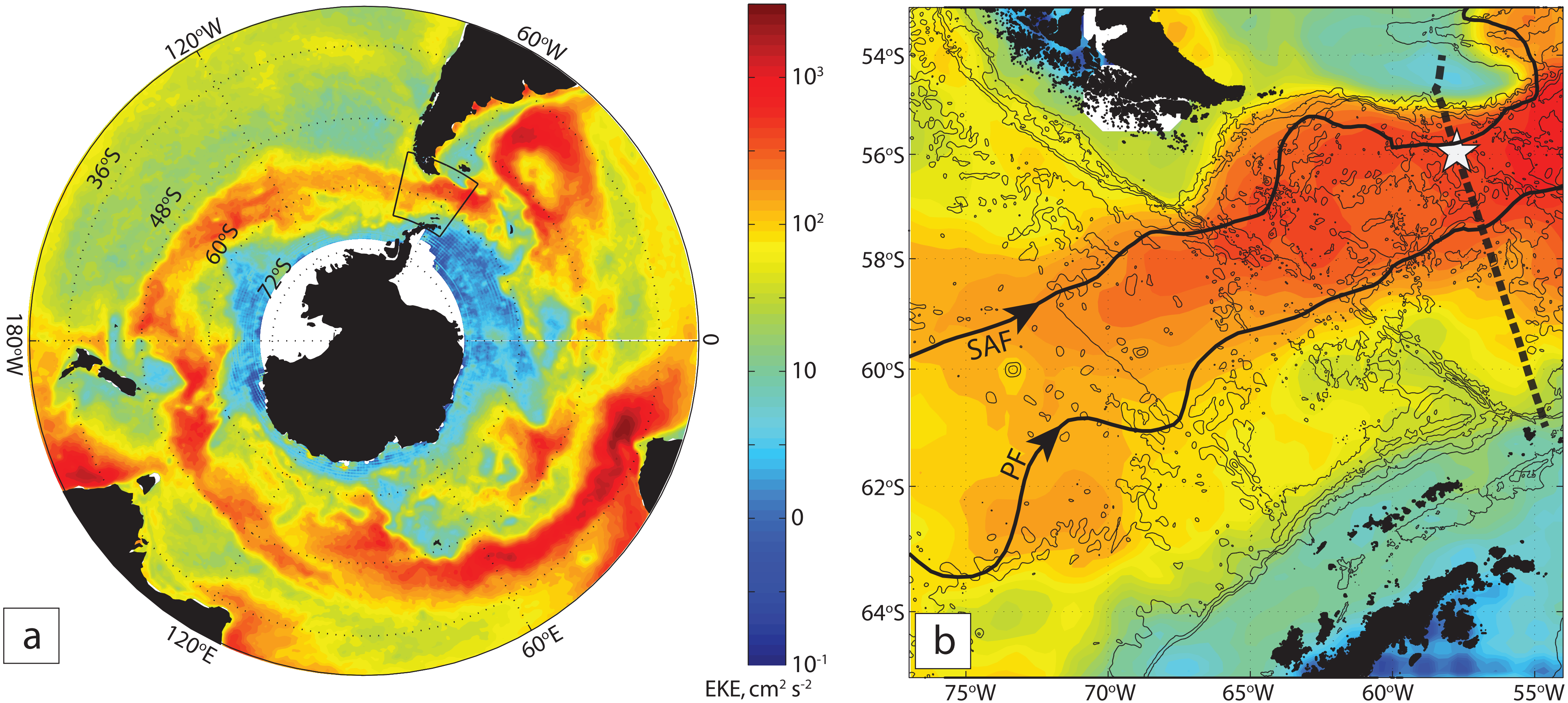

120°W
60°W
36°S
48°S
60°S
72°S
180°W
0
120°E
60°E
a
10^3
10^2
10
0
10^-1
EKE, cm^2 s^-2
54°S
56°S
58°S
60°S
62°S
64°S
SAF
PF
b
75°W
70°W
65°W
60°W
55°W

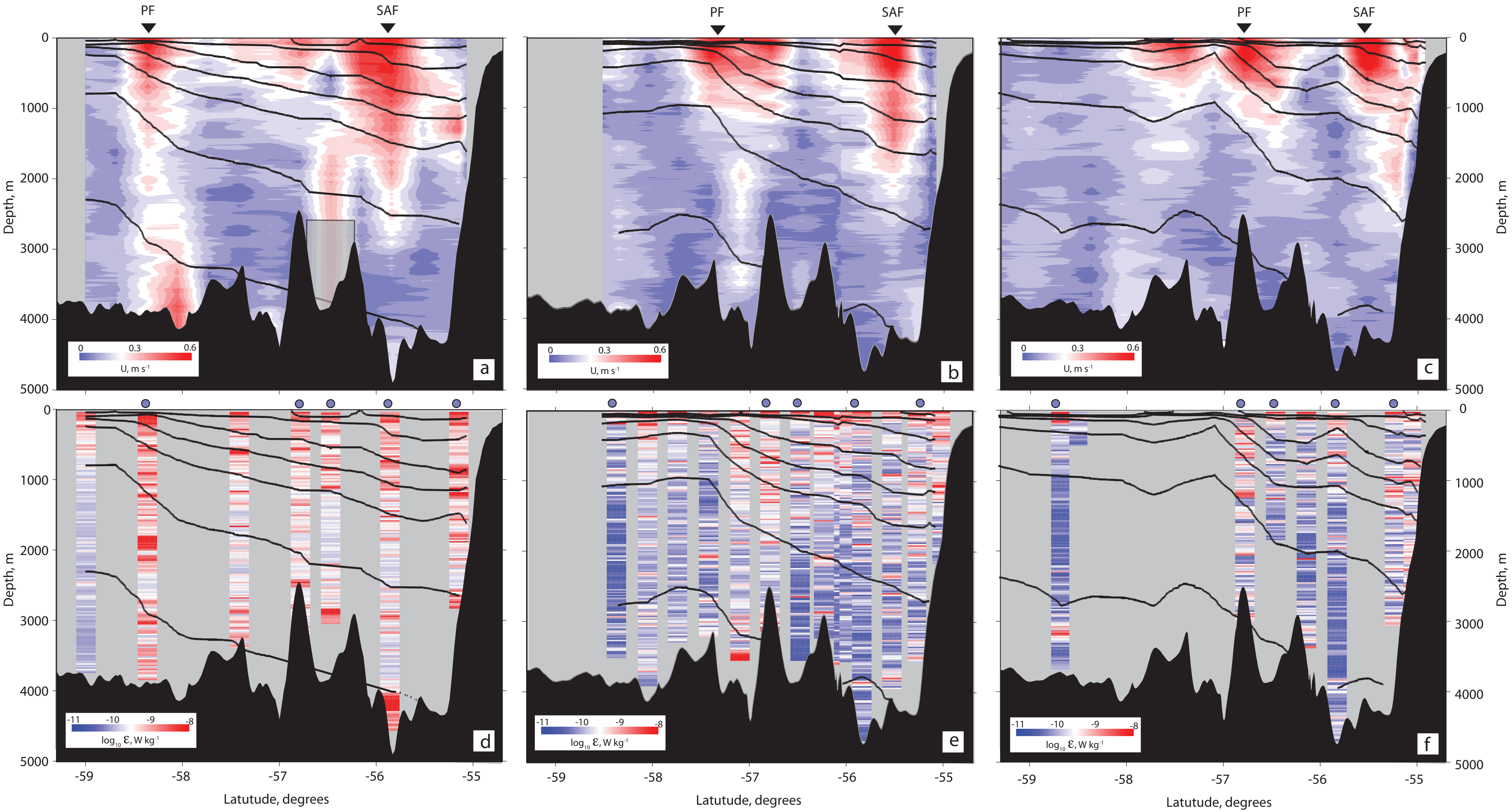
PF
SAF
a
b
c
d
e
f
Depth, m
U, m s-1
0
0.3
0.6
log10 ε, W kg-1
-11
-10
-9
-8
-59
-58
-57
-56
-55
Latutude, degrees
0
1000
2000
3000
4000
5000

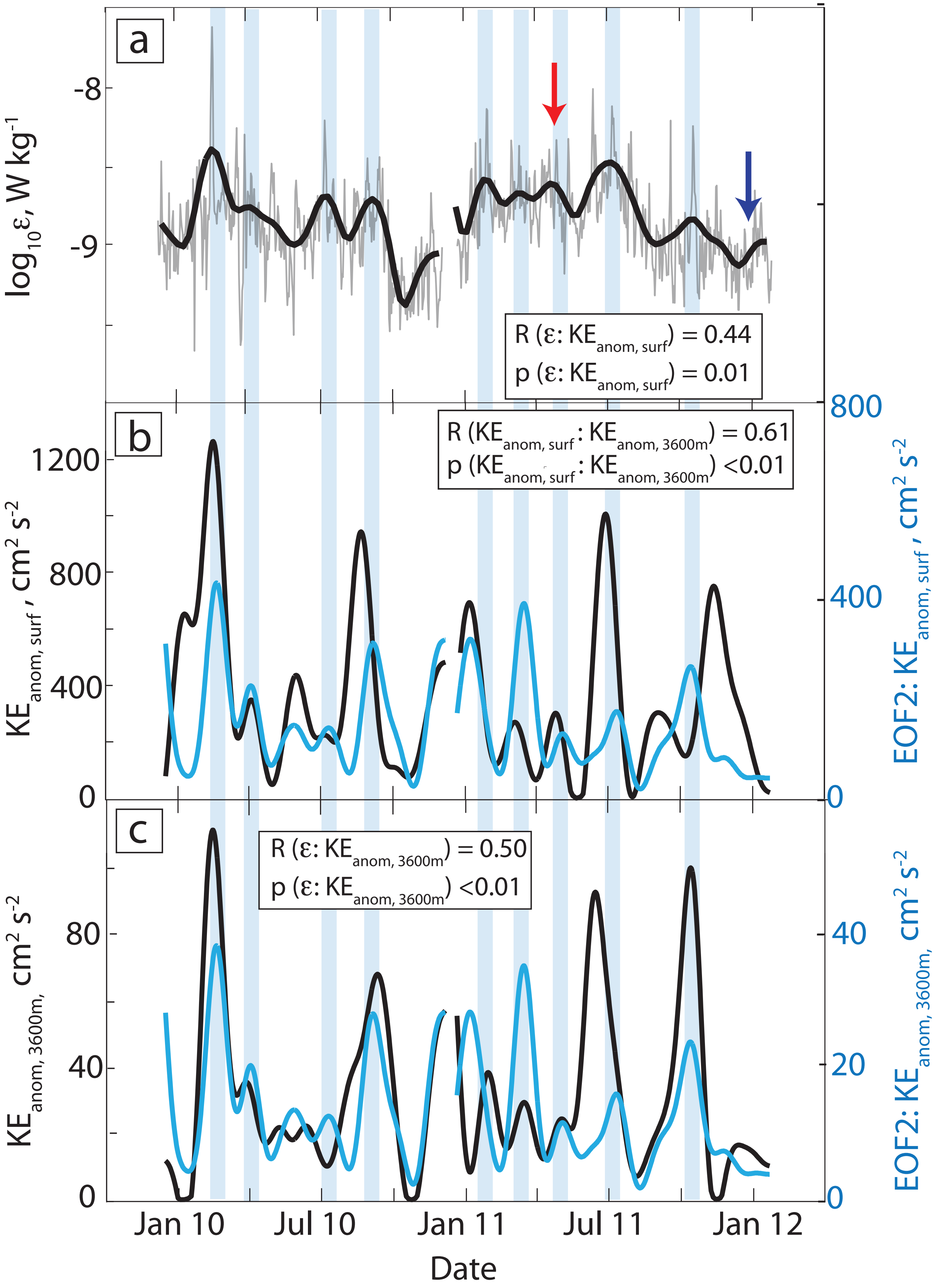

a
b
c
-8
-9
log10ε, W kg-1
R (ε: KEanom, surf) = 0.44
p (ε: KEanom, surf) = 0.01
R (KEanom, surf : KEanom, 3600m) = 0.61
p (KEanom, surf : KEanom, 3600m) <0.01
1200
800
400
0
KEanom, surf , cm2 s-2
800
400
0
EOF2: KEanom, surf , cm2 s-2
R (ε: KEanom, 3600m) = 0.50
p (ε: KEanom, 3600m) <0.01
80
40
0
KEanom, 3600m, cm2 s-2
40
20
0
EOF2: KEanom, 3600m, cm2 s-2
Jan 10
Jul 10
Jan 11
Jul 11
Jan 12
Date

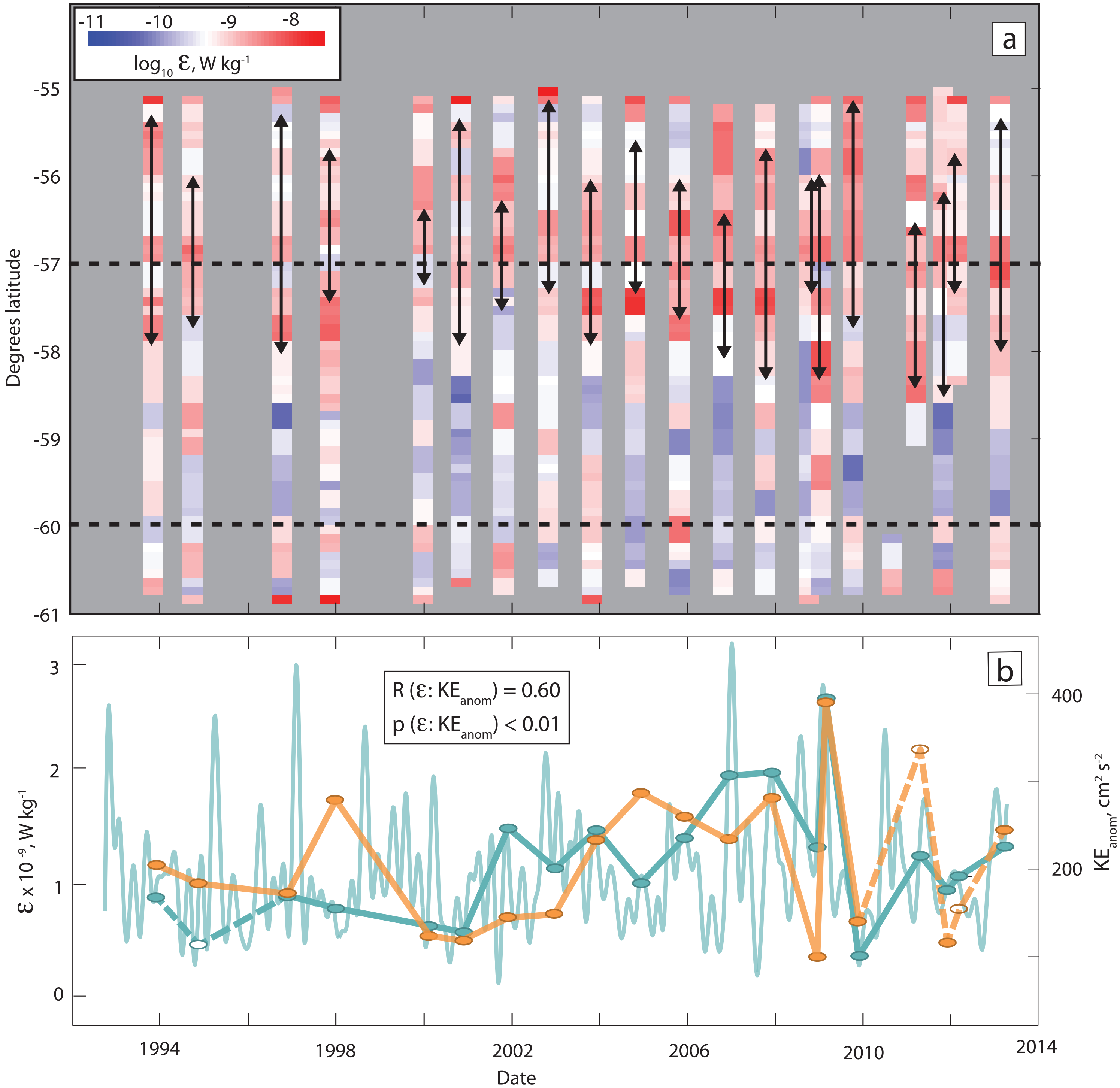
-11 -10 -9 -8
log10 ε, W kg-1
a
-55
-56
-57
-58
-59
-60
-61
Degrees latitude
b
R (ε: KEanom) = 0.60
p (ε: KEanom) < 0.01
3
2
1
0
ε x 10-9, W kg-1
400
200
KEanom, cm2 s-2
1994
1998
2002
2006
2010
2014
Date

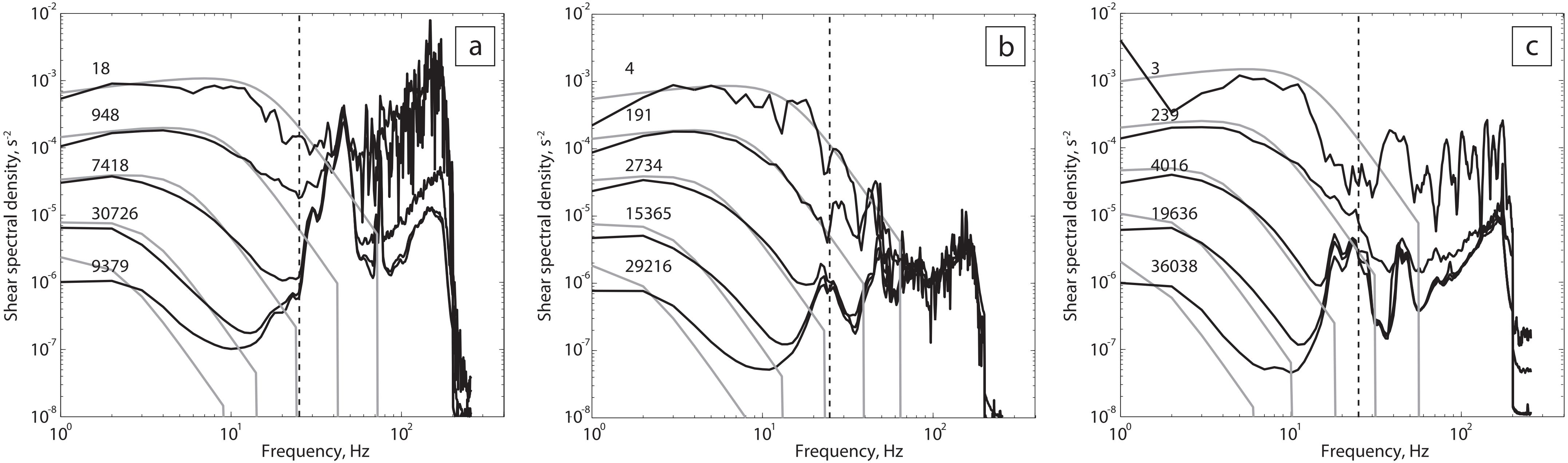

a
b
c
18
948
7418
30726
9379
4
191
2734
15365
29216
3
239
4016
19636
36038
Shear spectral density, s-2
Frequency, Hz

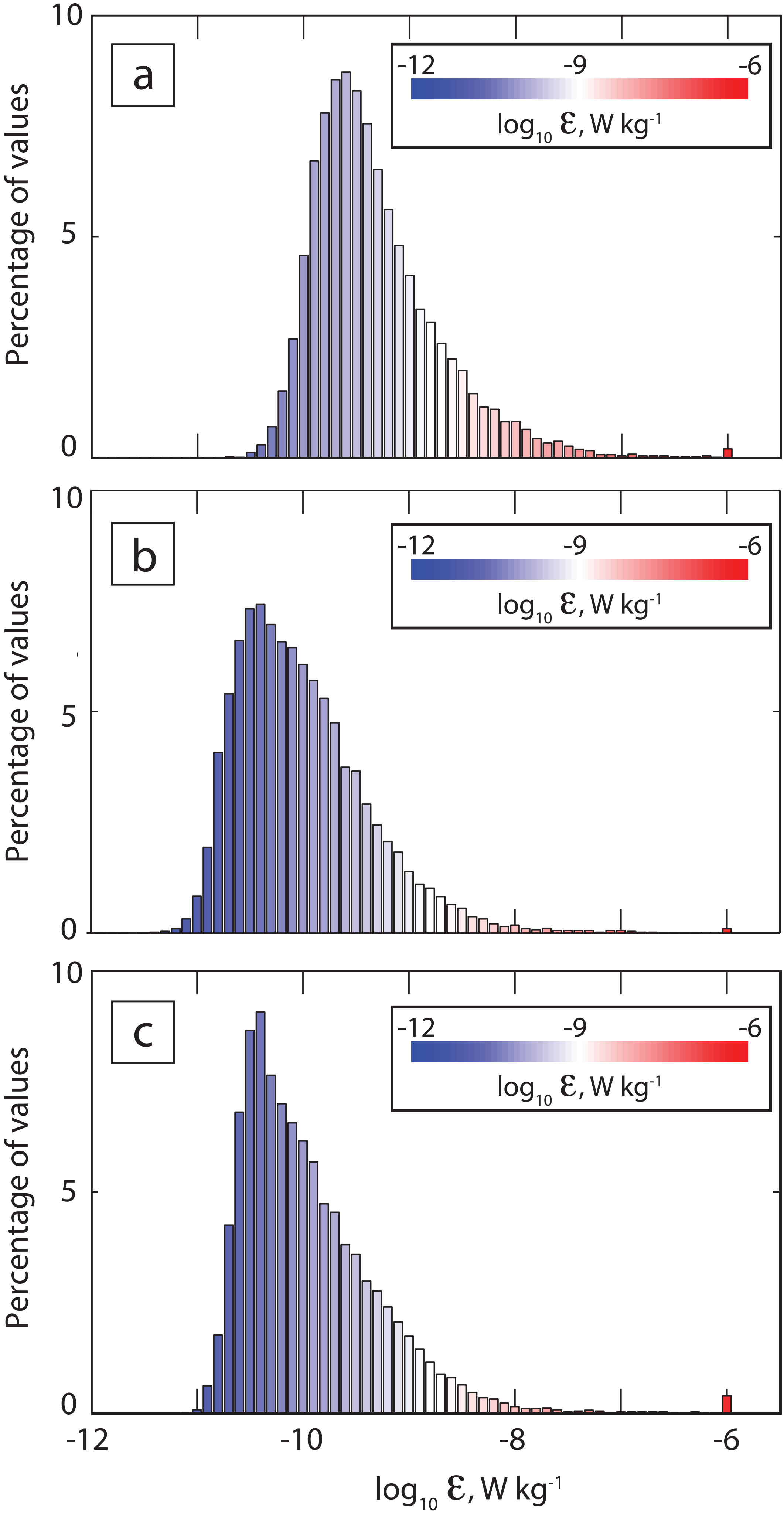
a
b
c
-12
-9
-6
log10 ε, W kg-1
Percentage of values
0
5
10
-12
-10
-8
-6
log10 ε, W kg-1

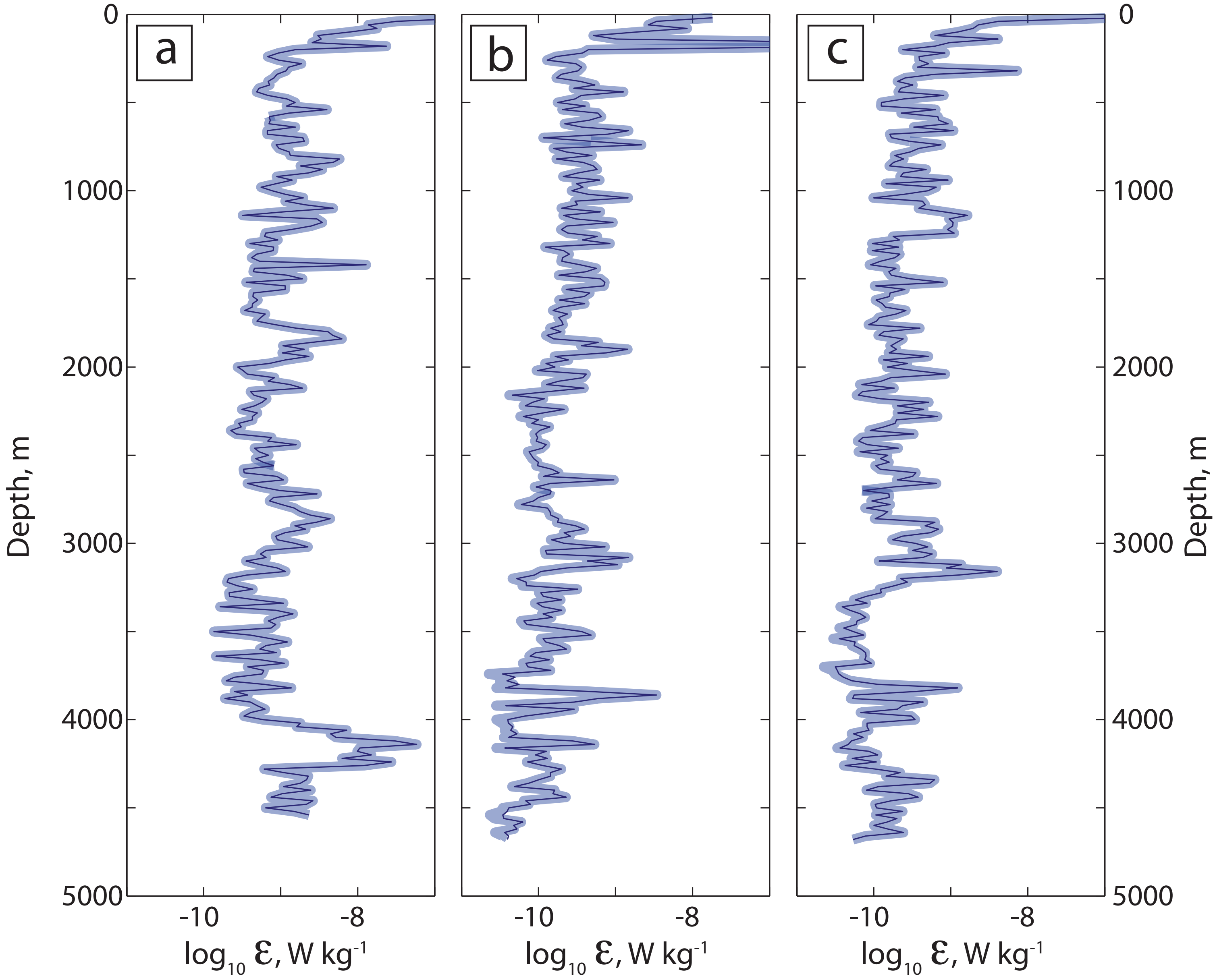
a
b
c
Depth, m
0
1000
2000
3000
4000
5000
-10
-8
log10 ε, W kg-1

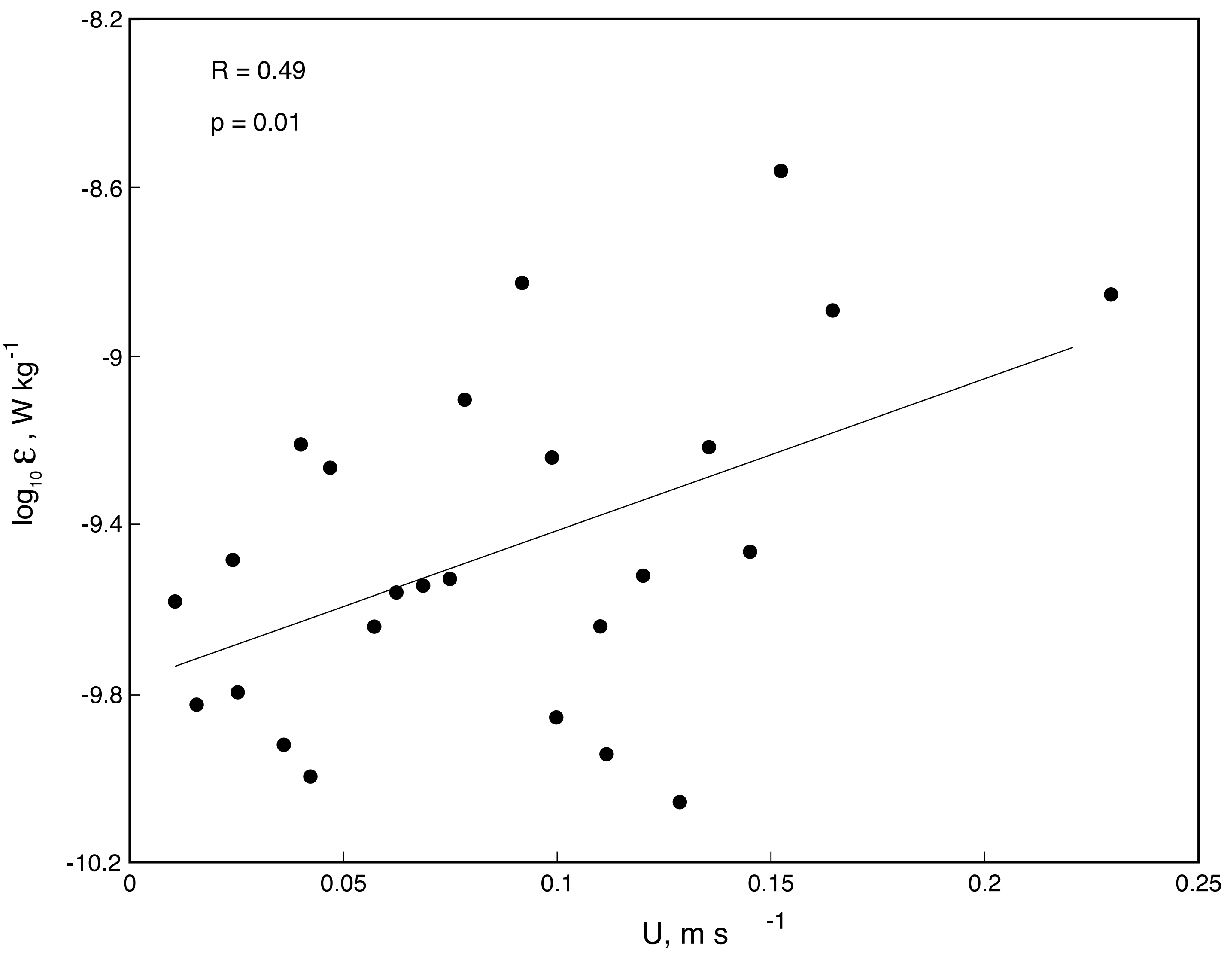

R = 0.49
p = 0.01
-8.2
-8.6
-9
-9.4
-9.8
-10.2
0
0.05
0.1
0.15
0.2
0.25
$\log_{10} \varepsilon$ , W kg$^{-1}$
U, m s$^{-1}$

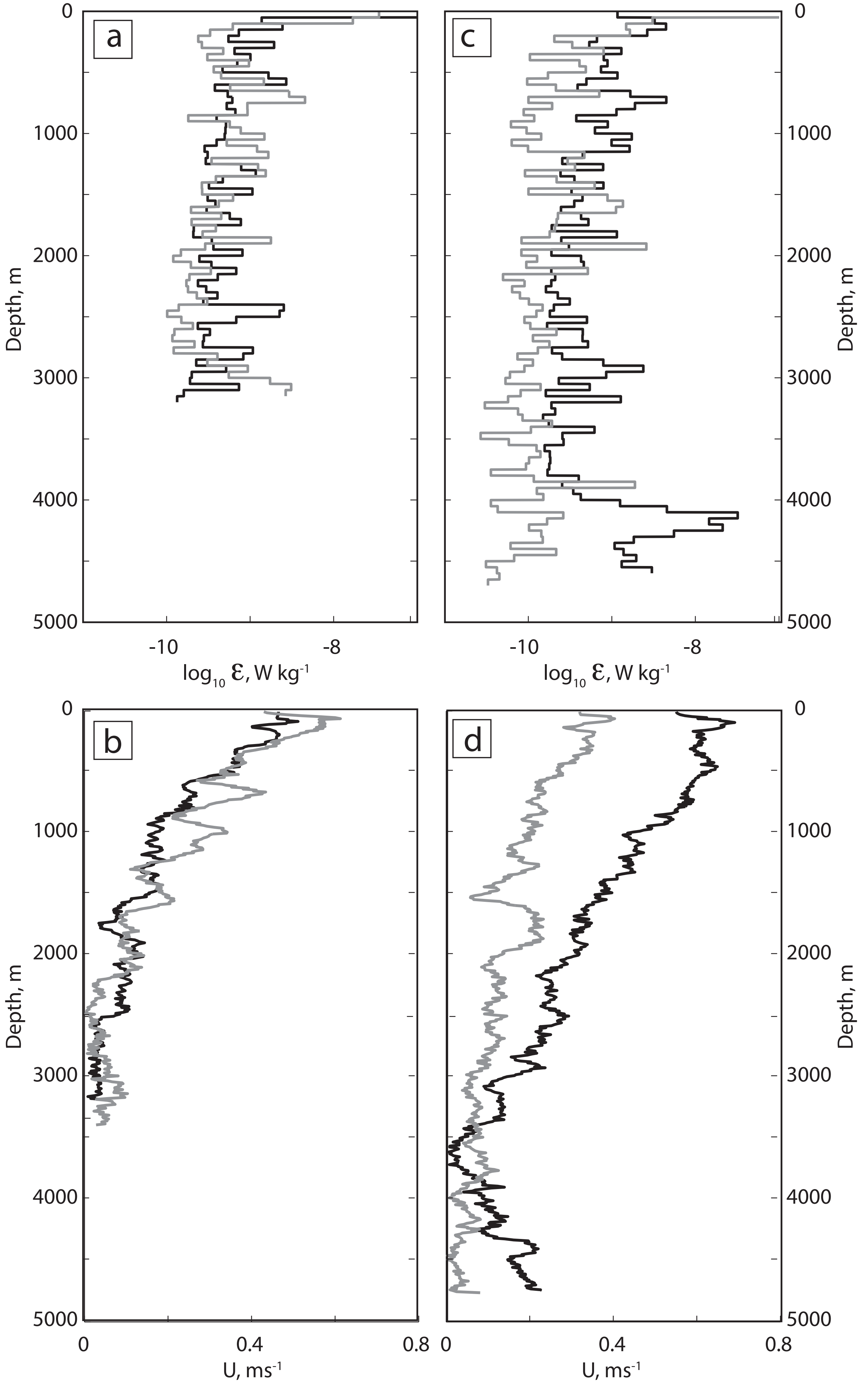
a
b
c
d
Depth, m
0
1000
2000
3000
4000
5000
-10
-8
log$_{10}$ ε, W kg$^{-1}$
0
0.4
0.8
U, ms$^{-1}$

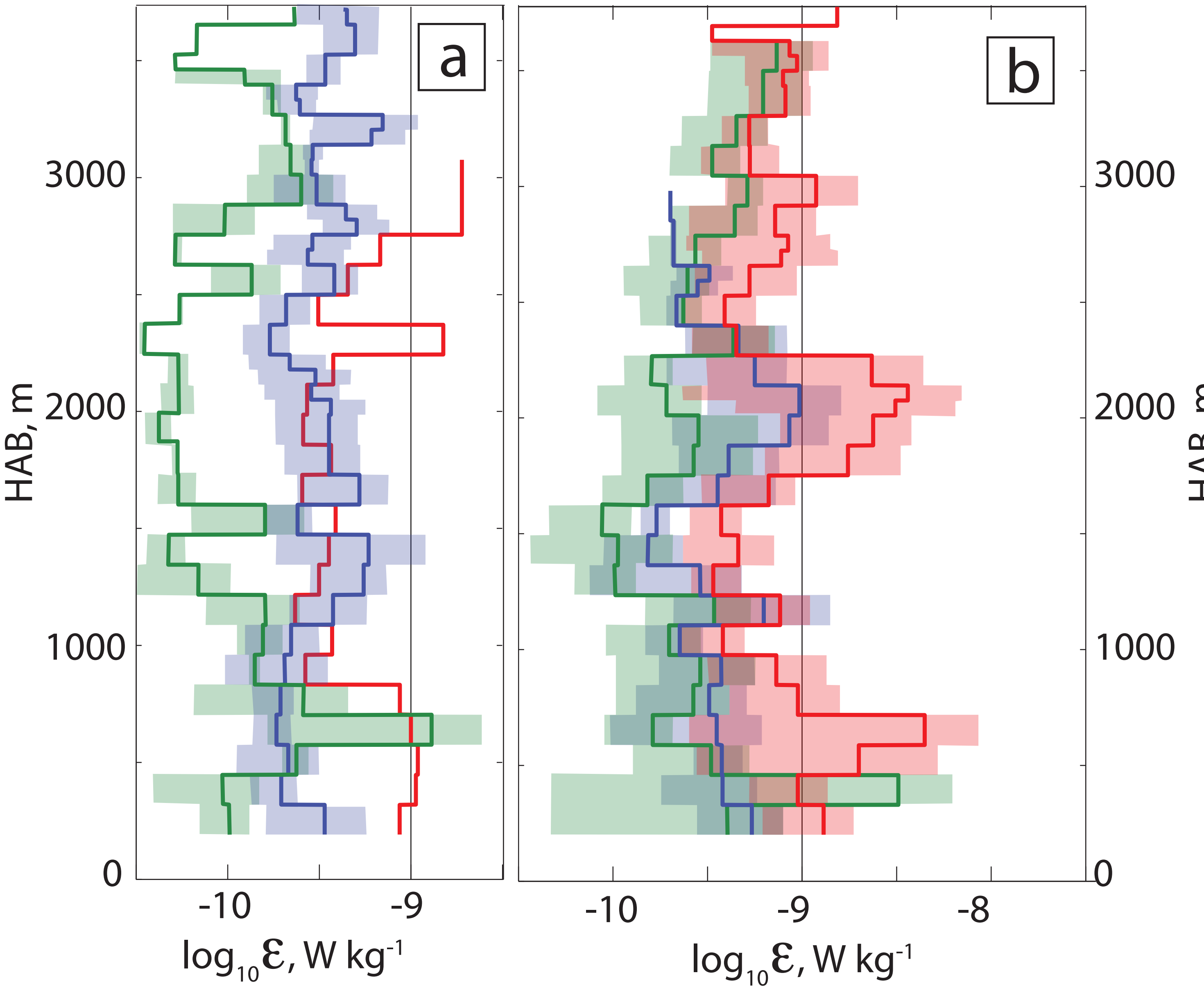
a
b
3000
2000
1000
0
HAB, m
-10
-9
-8
log$_{10}$ε, W kg$^{-1}$

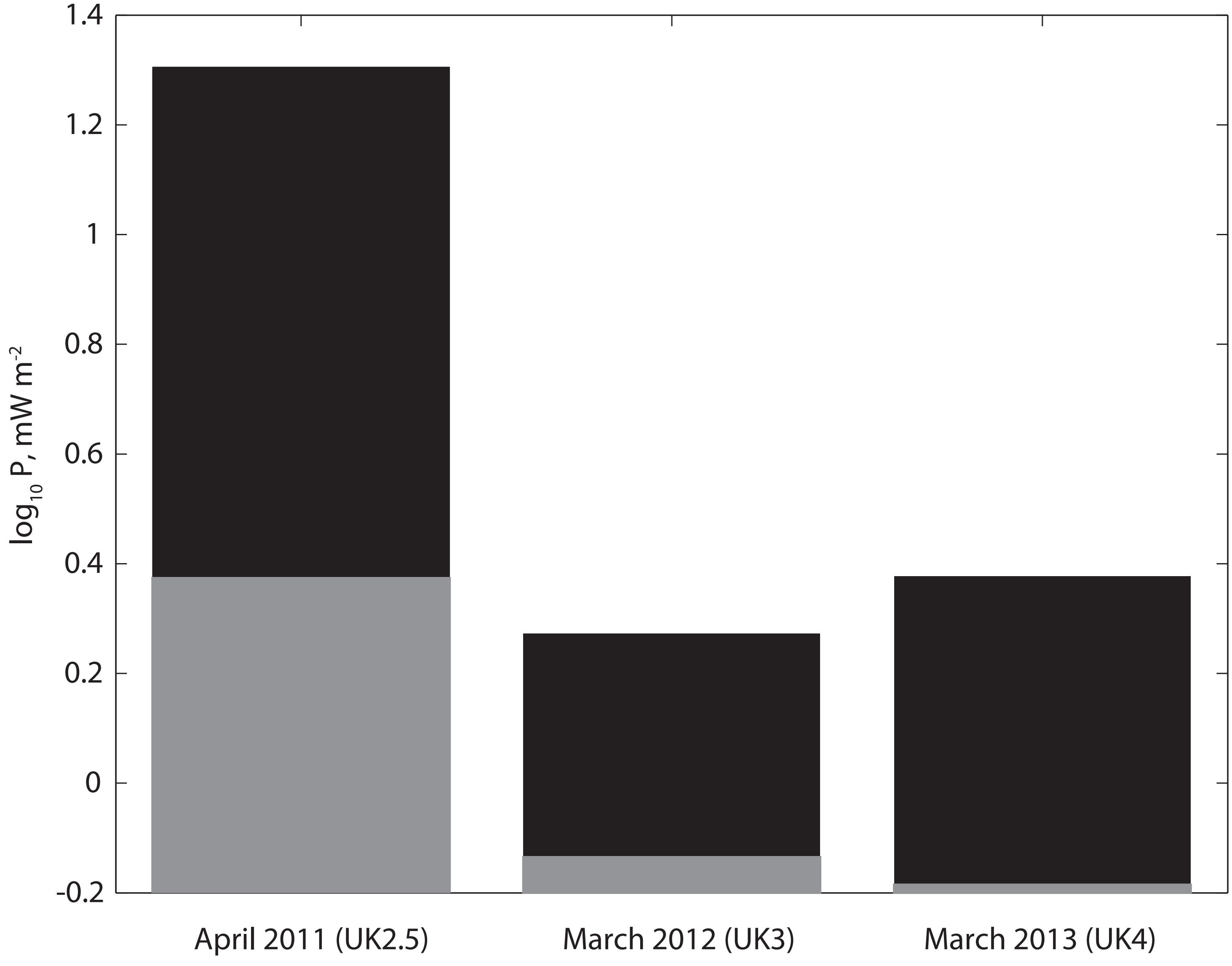
1.4
1.2
1
0.8
0.6
0.4
0.2
0
-0.2
$\log_{10}$ P, mW m$^{-2}$
April 2011 (UK2.5)
March 2012 (UK3)
March 2013 (UK4)

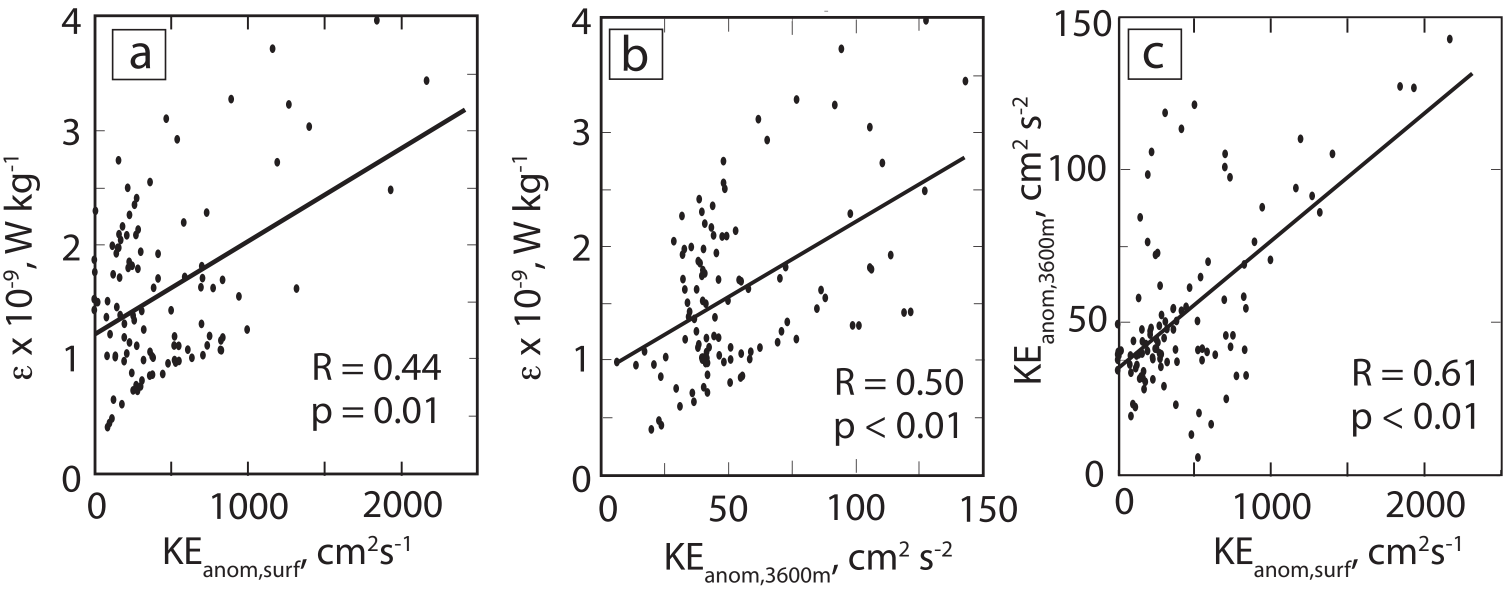

a
R = 0.44
p = 0.01
ε x 10^-9, W kg^-1
KE_anom,surf, cm^2s^-1
b
R = 0.50
p < 0.01
ε x 10^-9, W kg^-1
KE_anom,3600m, cm^2 s^-2
c
R = 0.61
p < 0.01
KE_anom,3600m, cm^2 s^-2
KE_anom,surf, cm^2s^-1

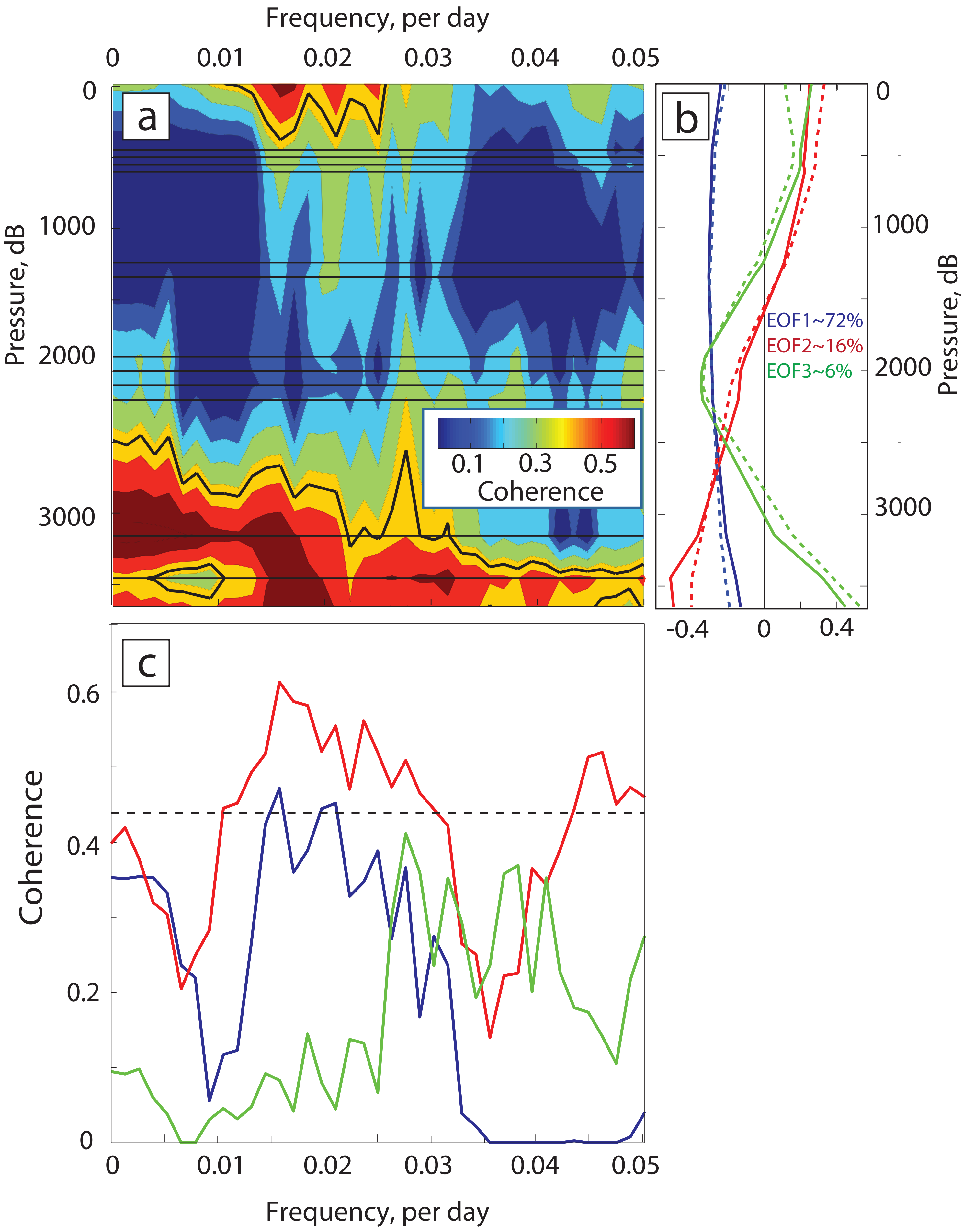

Frequency, per day
0
0.01
0.02
0.03
0.04
0.05
Pressure, dB
0
1000
2000
3000
a
0.1
0.3
0.5
Coherence
b
EOF1~72%
EOF2~16%
EOF3~6%
-0.4
0
0.4
c
Coherence
0.6
0.4
0.2
0
Frequency, per day

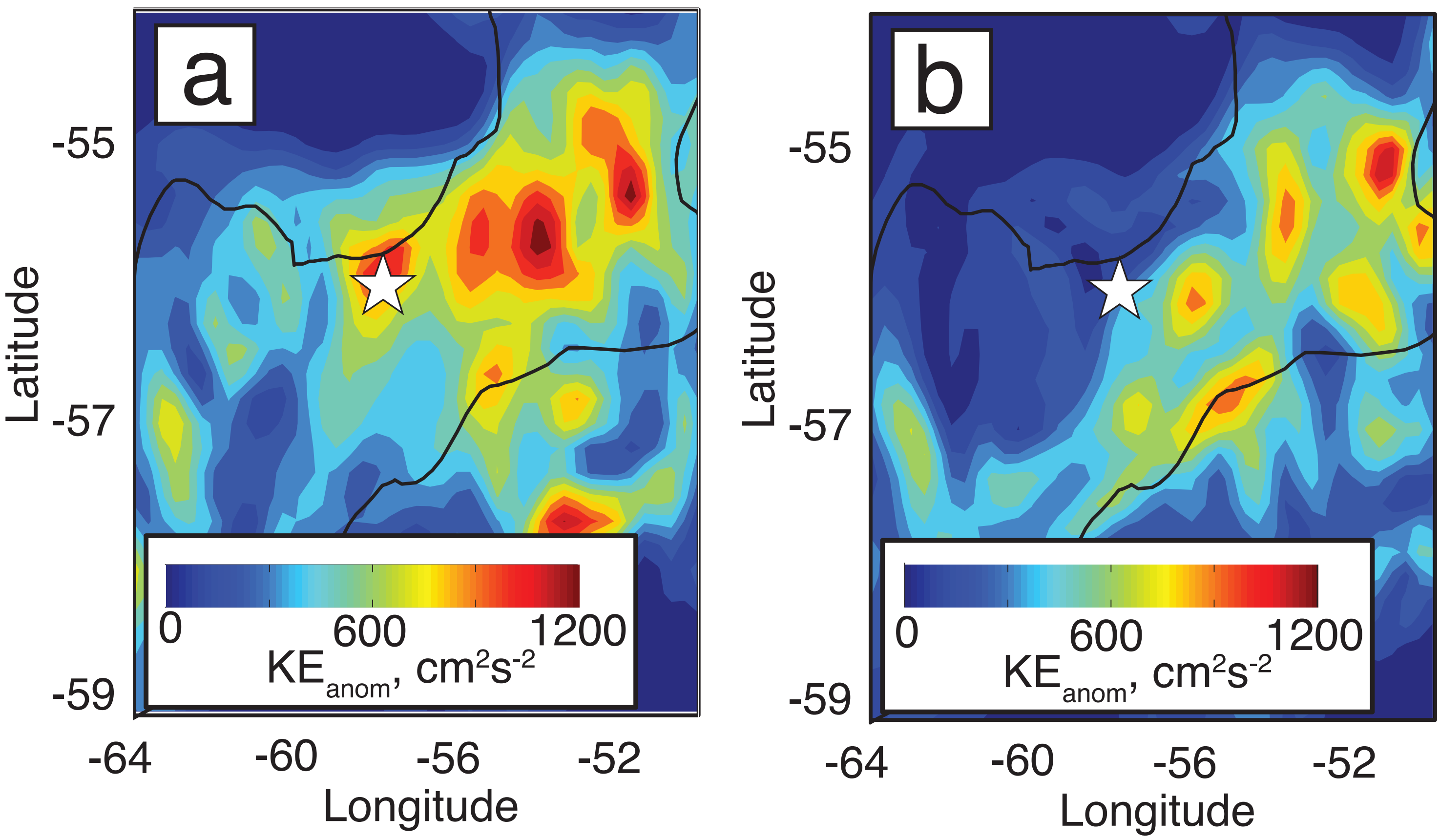
a
b
-55
-57
-59
Latitude
-64
-60
-56
-52
Longitude
0
600
1200
KE$_{anom}$, cm$^2$s$^{-2}$

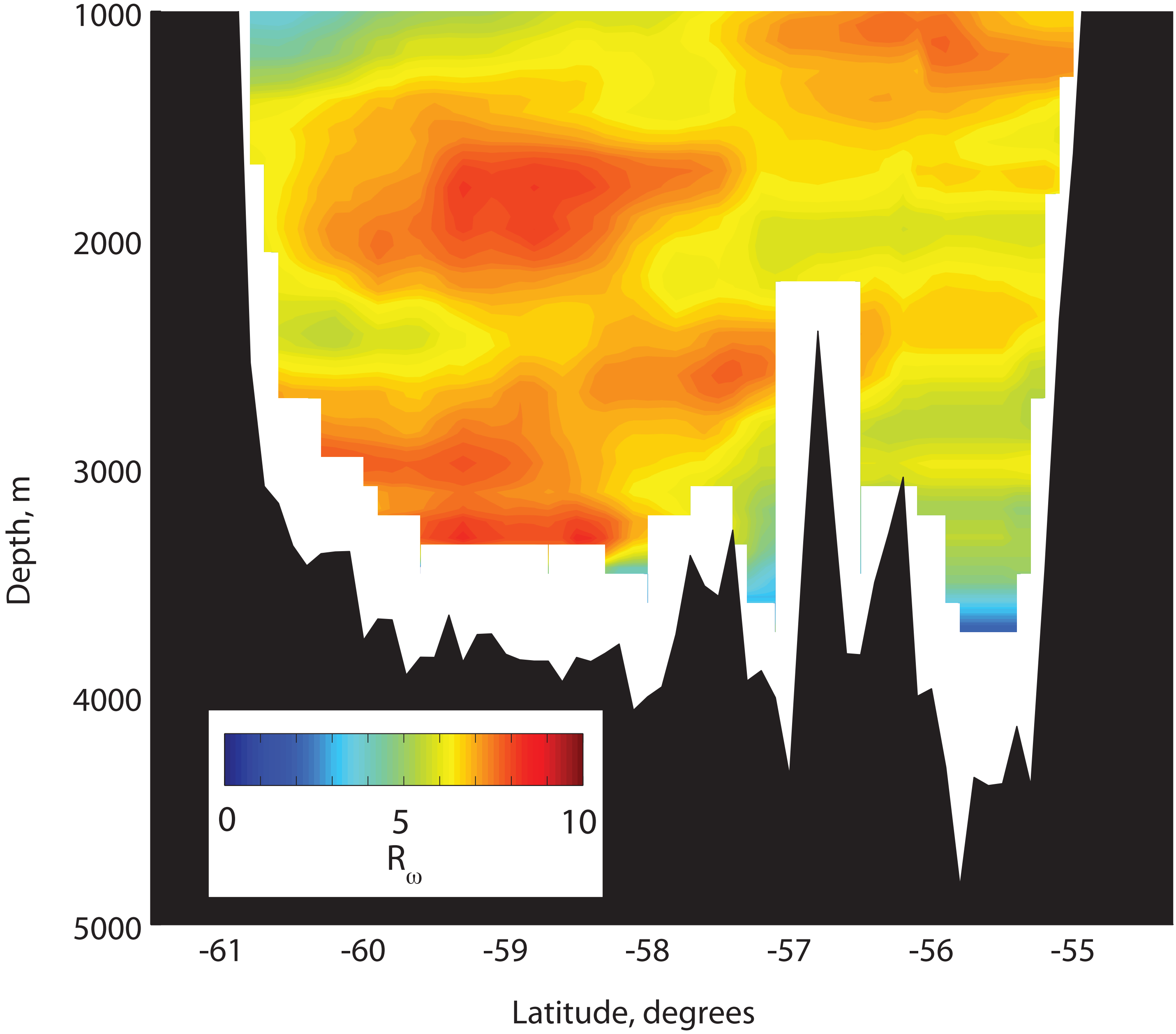

1000
2000
3000
4000
5000
Depth, m
-61
-60
-59
-58
-57
-56
-55
Latitude, degrees
0
5
10
$R_\omega$

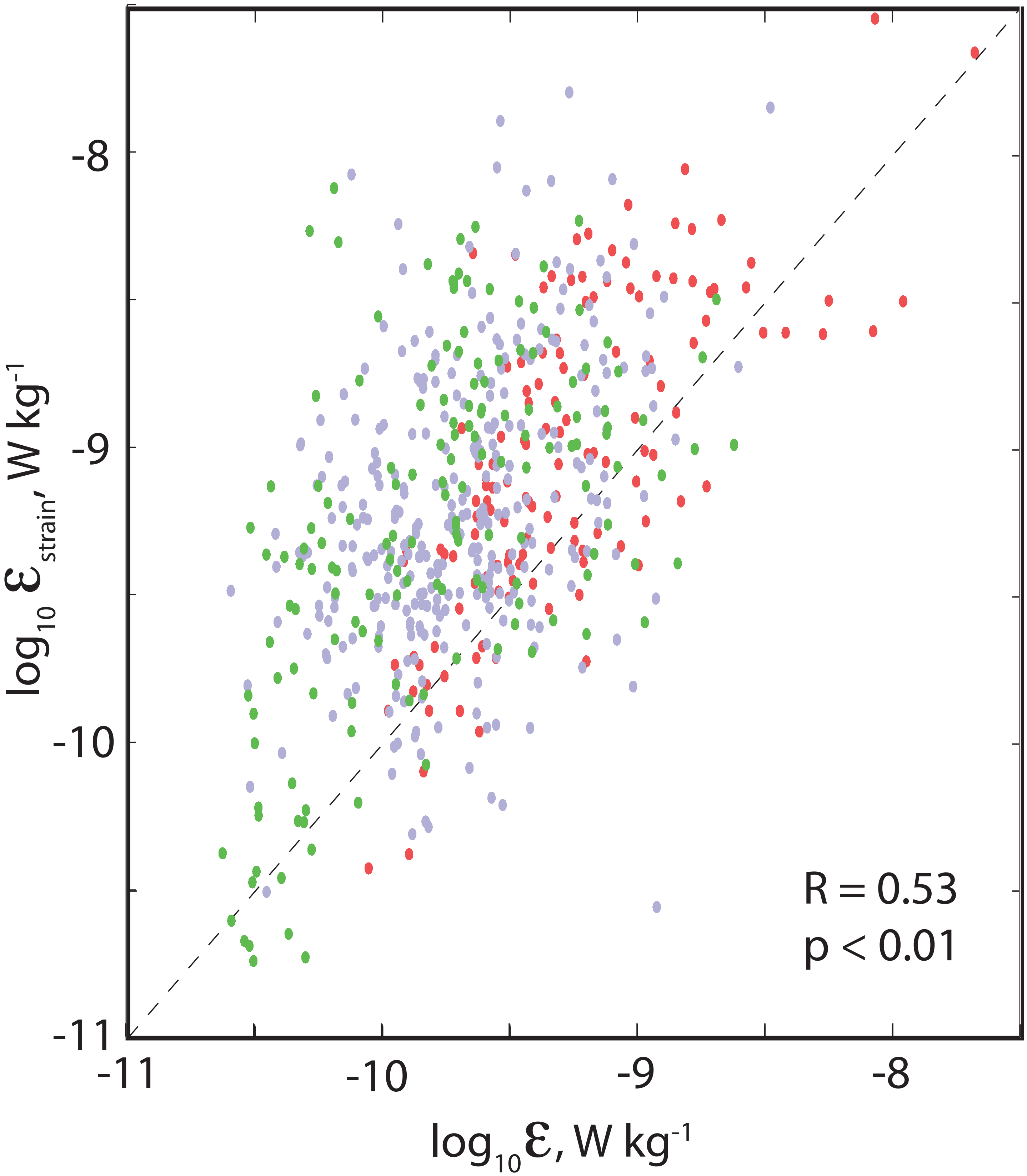

-8
-9
-10
-11
-11
-10
-9
-8
$\log_{10} \varepsilon_{strain}$, W kg$^{-1}$
$\log_{10} \varepsilon$, W kg$^{-1}$
R = 0.53
p < 0.01

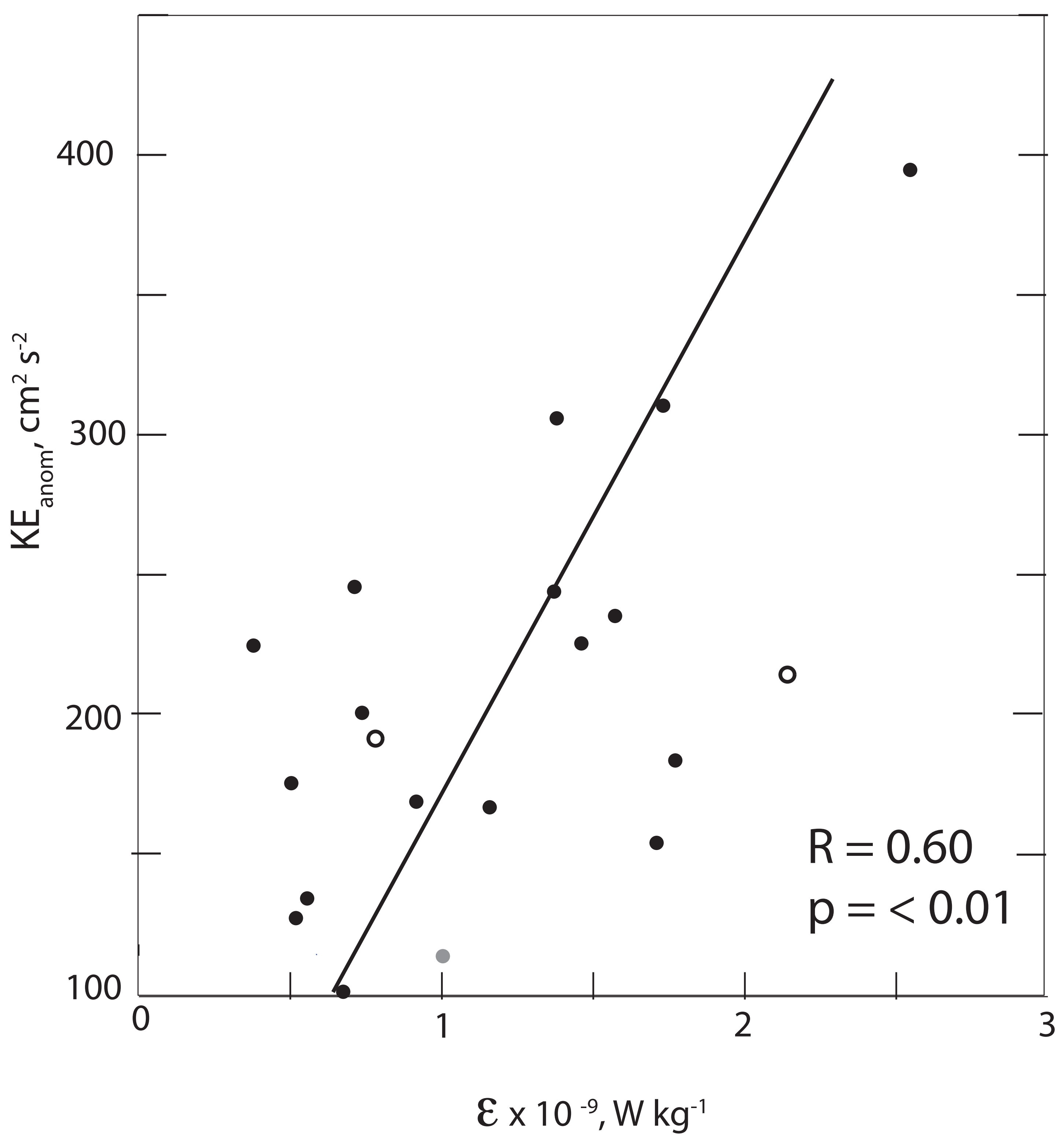

400
300
200
100
0
1
2
3
KE_anom, cm^2 s^-2
ε x 10^-9, W kg^-1
R = 0.60
p = < 0.01

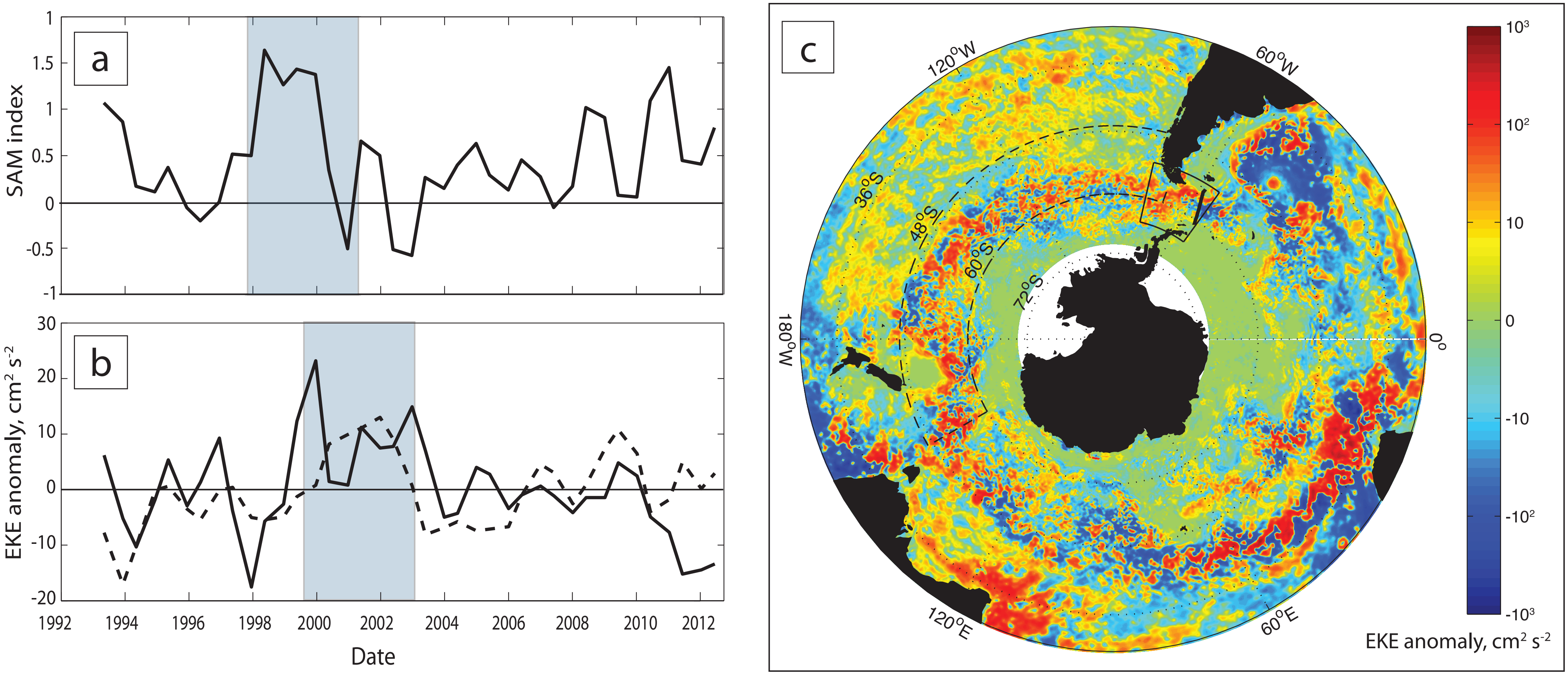
a
SAM index
b
EKE anomaly, cm² s⁻²
Date
c
120°W
60°W
36°S
48°S
60°S
72°S
180°W
0°
120°E
60°E
EKE anomaly, cm² s⁻²